Effect of Ca^{2+}/Sr^{2+} Substitution on the Electronic Structure of the Oxygen-Evolving Complex of Photosystem II: A Combined Multifrequency EPR, ^{55}Mn-ENDOR, and DFT Study of the S_2 State

Nicholas Cox,*[†] Leonid Rapatskiy,[†] Ji-Hu Su,[†] Dimitrios A. Pantazis,[†,‡] Miwa Sugiura,[§] Leonid Kulik,[∥] Pierre Dorlet,[⊥] A. William Rutherford,[⊥] Frank Neese,[†,‡] Alain Boussac,[⊥] Wolfgang Lubitz,*[†] and Johannes Messinger*,[#]

[†]Max-Planck-Institut für Bioanorganische Chemie, Stiftstrasse 34-36, D-45470 Mülheim an der Ruhr, Germany

[‡]Lehrstuhl für Theoretische Chemie, Institut für Physikalische und Theoretische Chemie, Universität Bonn, Wegelerstrasse 12, D-53115 Bonn, Germany

[§]Cell-Free Science and Technology Research Center, Ehime University, Bunkyo-cho, Matsuyama Ehime 790-8577, Japan

[∥]Institute of Chemical Kinetics and Combustion, Institutskaya 3, 630090 Novosibirsk, Russia

[⊥]iBiTec-S, URA CNRS 2096, CEA Saclay, 91191 Gif-sur-Yvette, France

[#]Department of Chemistry, Chemical Biological Centre (KBC), Umeå University, S-90187 Umeå, Sweden

S *Supporting Information*

ABSTRACT: The electronic structures of the native Mn_4O_xCa cluster and the biosynthetically substituted Mn_4O_xSr cluster of the oxygen evolving complex (OEC) of photosystem II (PSII) core complexes isolated from *Thermosynechococcus elongatus*, poised in the S_2 state, were studied by X- and Q-band CW-EPR and by pulsed Q-band ^{55}Mn-ENDOR spectroscopy. Both wild type and tyrosine D less mutants grown photoautotrophically in either $CaCl_2$ or $SrCl_2$ containing media were measured. The obtained CW-EPR spectra of the S_2 state displayed the characteristic, clearly noticeable differences in the hyperfine pattern of the multiline EPR signal [Boussac et al. *J. Biol. Chem.* **2004**, *279*, 22809−22819]. In sharp contrast, the manganese (^{55}Mn) ENDOR spectra of the Ca and Sr forms of the OEC were remarkably similar. Multifrequency simulations of the X- and Q-band CW-EPR and ^{55}Mn-pulsed ENDOR spectra using the Spin Hamiltonian formalism were performed to investigate this surprising result. It is shown that (i) all four manganese ions contribute to the ^{55}Mn-ENDOR spectra; (ii) only small changes are seen in the fitted isotropic hyperfine values for the Ca^{2+} and Sr^{2+} containing OEC, suggesting that there is no change in the overall spin distribution (electronic coupling scheme) upon Ca^{2+}/Sr^{2+} substitution; (iii) the changes in the CW-EPR hyperfine pattern can be explained by a small decrease in the anisotropy of at least two hyperfine tensors. It is proposed that modifications at the Ca^{2+} site may modulate the fine structure tensor of the Mn^{III} ion. DFT calculations support the above conclusions. Our data analysis also provides strong support for the notion that in the S_2 state the coordination of the Mn^{III} ion is square-pyramidal (5-coordinate) or octahedral (6-coordinate) with tetragonal elongation. In addition, it is shown that only one of the currently published OEC models, the Siegbahn structure [Siegbahn, P. E. M. *Acc. Chem. Res.* **2009**, *42*, 1871−1880, Pantazis, D. A. et al. *Phys. Chem. Chem. Phys.* **2009**, *11*, 6788−6798], is consistent with all data presented here. These results provide important information for the structure of the OEC and the water-splitting mechanism. In particular, the 5-coordinate Mn^{III} is a potential site for substrate 'water' (H_2O, OH^-) binding. Its location within the cuboidal structural unit, as opposed to the external 'dangler' position, may have important consequences for the mechanism of O−O bond formation.
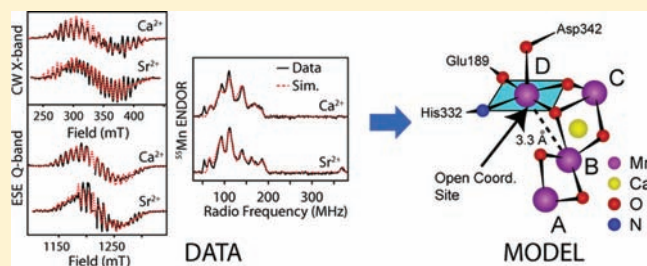
1. INTRODUCTION

In oxygenic photosynthesis light-driven water-splitting is catalyzed by the oxygen-evolving complex (OEC) of Photosystem II (PSII). The OEC consists of an inorganic Mn_4O_xCa cluster (where $4 \leq x \leq 6$ indicates the number of oxygen bridges) and its surrounding protein matrix.[1−14] The functionally important protein matrix includes the redox-active tyrosine residue Y_Z (D_1-Y_{161}). Y_Z couples electron transfer from the Mn_4O_xCa cluster to P_{680} and is involved in proton transfer reactions.[15] $P_{680}/P_{680}^{•+}$ and Pheo/Pheo$^{•-}$ form the primary component of the photoactive reaction center of PSII, which energetically drives water-splitting by four sequential light-induced charge separations, for reviews see refs 8−14, and 16−18. During
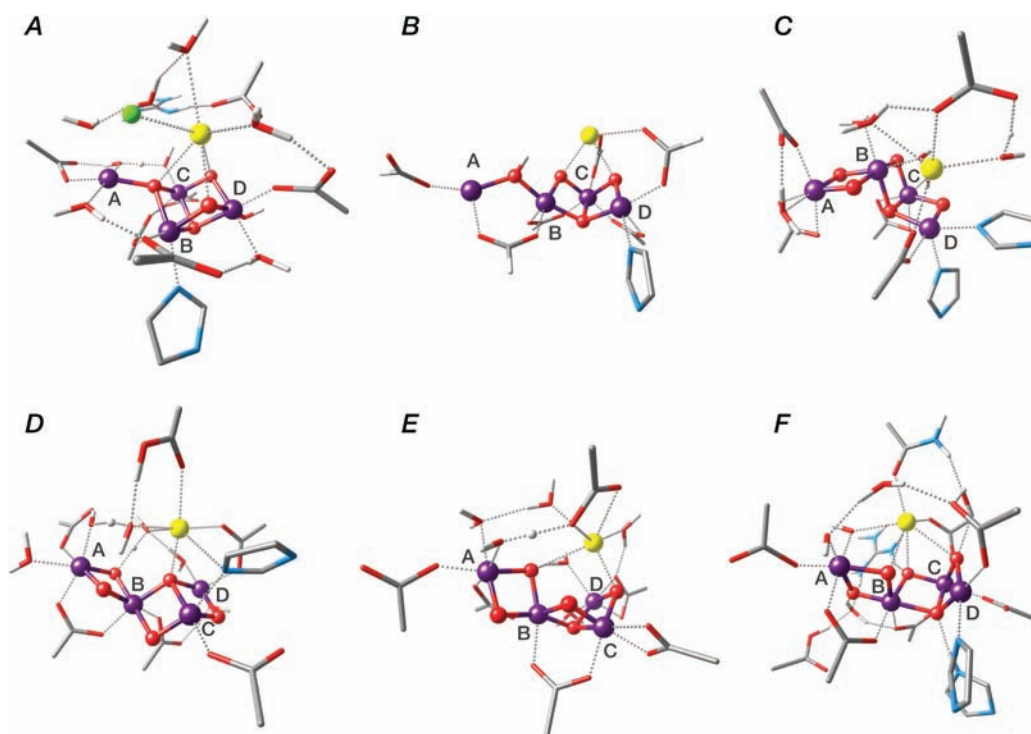
Figure 1. Current QM/MM and DFT literature models for the OEC poised in the S_2 state based on recent X-ray crystallographic[3–5] and polarized EXAFS[6,7] data. A) London crystal structure;[3,43–45] B) Berlin crystal structure;[4,5,53,54] C) EXAFS core I;[6,57] D) EXAFS core II;[6,57] E) EXAFS core III;[6,57] F) Siegbahn model.[11,58,59] Purple spheres: manganese; red: oxygens; yellow: calcium; green: chloride; blue: nitrogen; gray: carbon.

Scheme 1
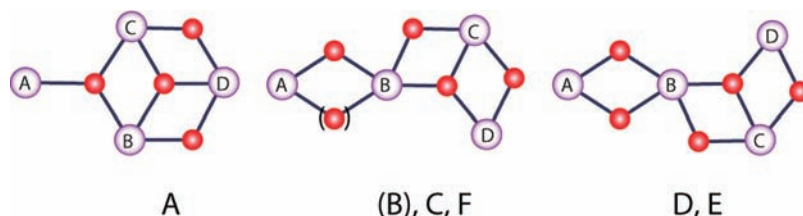
water-splitting, the Mn_4O_xCa cluster steps through a reaction cycle comprising five distinct redox intermediates. These are known as the S_n states, where the index indicates the number of stored oxidizing equivalents $(n = 0–4)$.[19] Once formed the $S_3Y_Z^\bullet$ rapidly decays to the S_0 state upon the release of molecular triplet oxygen and the rebinding of at least one substrate water molecule.[9,10] A S_4 state, which is different from $S_3Y_Z^\bullet$, has not yet been spectroscopically identified.

Ca^{2+} is known to be an essential cofactor for the water-splitting reaction.[20–25] Removal of Ca^{2+} inhibits water-splitting by blocking the $S_2 \rightarrow S_3$ transition.[26] It was demonstrated that Sr^{2+} is the only surrogate that is able of restoring water-splitting after Ca^{2+} removal, albeit at a slower turnover rate.[23,26,27] It has been speculated that this may be due to a combination of two important factors. The surrogate must match: (i) the approximate size and (ii) the Lewis acidity[28] of Ca^{2+}. This suggests a role for Ca/Sr in substrate water binding. Time-resolved $H_2^{16}O/H_2^{18}O$ exchange measurements performed by membrane-inlet mass spectrometry[29,30] demonstrate that the exchange kinetics of the slowly exchanging substrate water molecule are strongly affected by Ca/Sr exchange.[31,32]

It has been recently shown that the thermophilic cyanobacterium *Thermosynechococcus elongatus* (*T. elongatus*) can be photoautotrophically grown in either Ca^{2+} or Sr^{2+} containing media. It is thus possible to obtain PSII complexes with intact Mn_4O_xCa or Mn_4O_xSr clusters that display high oxygen-evolving activities.[27,33,34] Consistent with these high activities, only minor structural differences — mainly in $Mn-Ca^{2+}/Sr^{2+}$ distances - are observed in the S_1 and S_2 states between these two sample types by EXAFS spectroscopy.[35] The physical proximity of the Ca^{2+} to the Mn cluster was first demonstrated by Mn K-edge EXAFS measurements on isotropic PSII samples[35–40] and then refined by X-ray crystallographic data[3–5,33] and polarized EXAFS.[6,7,41] Figure 1 summarizes current structural models of the Mn_4O_xCa cluster that are based on these approaches.[42] The manganese connectivity and labeling for the models of Figure 1 is depicted in Scheme 1 in which it can be seen that apart from model A, all other models share the same basic topology. It is noted however that model B lacks one μ-oxo linkage between Mn_A and Mn_B.

Model A is based on the London crystal structure and QM/MM and DFT based refinements.[3,43–45] Here the Ca^{2+} was

assigned as a vertex of a μ-oxo-bridged cubane-like structure, with three Mn defining the other three vertices. They form the three short (about 2.7 Å) Mn−Mn distances known from EXAFS spectroscopy.[46−48] Ca^{2+} is suggested to bind the slowly exchanging substrate water and a Cl^- ion. This is in conflict with recent crystallographic and spectroscopic data, which both demonstrate that the shortest Cl^- to metal distance is >5 Å in dark-adapted samples.[5,49−52] The fourth 'dangler' or outer Mn is attached to this core structure via a μ_4-oxo-bridged ligation to one of the oxygen corners of the cube and thereby forms the long (3.3 Å) Mn−Mn distance known from EXAFS spectroscopy.[46−48] Water-oxidation chemistry in these models was suggested to occur between one water bound to Ca and one that is bound as a terminal oxo to the outer Mn ion (Mn_A). Model B is based on the Berlin crystal structure[4] and was also refined by DFT calculations. In contrast to model A it has an open and flattened cube structure (one corner oxygen is missing), and the outer Mn is attached via one mono μ_2-oxo bridge. Ca^{2+} is suggested to coordinate to two μ_2-oxo bridges of the open cube; required protein ligands are not completely included in this minimal model[53,54] but see Kusunoki for a similar, more complete model.[55] Water-oxidation chemistry may occur in such models for example between two water molecules bound to the outer Mn (Mn_A).[55] Models C, D, and E of Figure 1 are based on structures (models I, II, and III, respectively) derived from polarized EXAFS measurements on PSII single crystals[6] that were further refined based on crystallographic information on possible ligands and DFT calculations.[56,57] These models also have a more planar geometry and are somewhat reminiscent of the original Berkeley 'dimer of dimers' model.[47] However, they are more interconnected than this original suggestion and have one additional 2.7 Å Mn−Mn distance[48] that is formed by connecting the di-μ-oxo bridge of one 'dimer' to a Mn of the other 'dimer'. Importantly, the symmetry of the cuboidal Mn_3O_3-Ca part is broken by the absence of one corner oxygen, which leads to a longer Mn−Mn distance of 3.3 Å inside this segment.[6] In model C, the Ca^{2+} is ligated in a similar fashion to the Mn_4O_x core as in model B, while in model D, the Ca^{2+} only has contact with the rest of the Mn cluster via its binding to the μ_3-oxo bridge connecting the Mn ions of the trimeric part. In model E the Ca^{2+} connects to two μ_2-oxo bridges: to one of the oxo's of the trimeric unit and to one of the bridges to the outer Mn ion. The most detailed and rigorous proposal at present is shown in Figure 1F.[11,58,59] The model of Siegbahn combines many crystallographic and spectroscopic data. It was designed to be of the lowest possible total energy and to allow low energy barrier O−O bond formation to occur between a hydroxo that binds to Mn_C in the S_3 state (which is 5 coordinated in the S_0 to S_2 states) and the μ_3-oxo bridge connecting Mn_A, Mn_B, and Ca. This model has strong similarities to models C and E but is more compact. In this model Ca is connected to all four Mn ions via three μ_2-oxo bridges. Recently a model related to models C, E, and F was proposed based on molecular mechanics modeling of the Berlin crystal structure[4] and comparison to polarized EXAFS data. Here two long (3.2 Å) Mn−Mn distances are assumed to be within the cuboidal part in the S_0, S_1, and S_2 states (between Mn_C-Mn_D and Mn_C-Mn_B), that shorten (to about 2.7 Å) during the $S_2{\rightarrow}S_3$ transition due to the oxidation of Mn_C^{III} and concomitant formation of another oxo bridge. As a consequence, water-oxidation is expected to occur between waters bound at the Mn_A and to Ca since all other manganese are coordinatively saturated in S_3 and S_4.[60,61]

As water oxidation involves four single oxidation events of the Mn_4O_xCa cluster during the S_n state cycle, it is particularly well suited for study by EPR. By using standard perpendicular mode CW-EPR the OEC in the S_2 state exhibits a characteristic multiline signal ($S = 1/2$, see below) as well as a broad signal at $g = 4.1$ ($S = 5/2$)[62] under certain sample conditions. Pulse EPR techniques have further advanced our understanding of the S_2 multiline state in higher plant (spinach).[63−67] In particular, [55]Mn-ENDOR has allowed the unambiguous determination of all four [55]Mn-hyperfine tensors and has thus made it possible to probe Mn-coupling schemes, which necessarily reflect the structure of the OEC, demonstrating that (i) all four Mn are strongly coupled ($|J| > 10$ cm^{-1}) and (ii) the most likely oxidation state of the Mn cluster in the S_2 state is $Mn^{III}(Mn^{IV})_3$,[65] consistent with XANES data (for review see ref 47).

The Sr^{2+} containing OEC, poised in the S_2 state, has been first studied in higher plant (spinach) BBY type preparations.[26] In these samples the Ca^{2+} is chemically removed by a low pH treatment, citric acid at pH 3,[20,68] or by NaCl/EDTA washing.[21,22] Supplemented Sr^{2+} then binds at the Ca^{2+} site, restoring the catalytic activity of the OEC albeit at a slower turnover rate.[26] The removal of Ca^{2+} and the subsequent introduction of Sr^{2+} into the Ca^{2+} site leads to a significant modification of the S_2 multiline EPR signal[26] Here we use photoautotrophically grown Ca^{2+}- and Sr^{2+}- from *T. elongatus* to further refine current models of the electronic structure of the paramagnetic S_2-state of the OEC.

2. MATERIALS AND METHODS

2.1. PSII Sample Preparation. Ca^{2+}/Sr^{2+} PSII core complex preparations from WT* *T. elongatus*[69] and from a TyrD less mutant[70] were isolated as described earlier.[27,34] Dark-adapted samples (~10 mg chlorophyll/mL) containing ~0.5 mM phenyl-para benzoquinone (PPBQ) and ~3% methanol were placed in Q-band quartz tubes with 3 mm outer diameter. The S_2-state was generated by short, white light illumination (5 s) at 200 K (dry ice/ethanol bath).

2.2. EPR Measurements. X-band CW-EPR spectra were recorded at 8.5 K using a Bruker ELEXSYS E500 X-band spectrometer equipped with an Oxford Instruments cryostat. For these measurements the Q-band tube was inserted into a X-band tube. Q-band pulse EPR and [55]Mn-Davies ENDOR measurements were performed at 4.2 K using a Bruker ELEXSYS E580 Q-band pulse EPR spectrometer equipped with an Oxford-CF935 liquid helium cryostat and an ITC-503 temperature controller. Electron spin echo-detected (ESE) field-swept spectra were measured using the pulse sequence: $\pi/2-\tau-\pi-\tau-$echo, where $\pi = 80$ ns and $\tau = 440$ ns. [55]Mn-Davies ENDOR spectra were collected using the pulse sequence: $\pi-\pi_{RF}-T-\pi/2-\tau-\pi-\tau-$echo, where $\pi = 80$ ns, $\tau = 440$ ns, π_{RF} (RF pulse, radio frequency) = 3.5 μs, and a delay $T = 600$ ns. To measure hyperfine couplings in excess of 150 MHz, a home-built computer console (SpecMan control software[63,64,71]) was used coupled to a external RF generator (SMT02 signal generator) and RF amplifier (ENI 5100 L). A shot repetition rate of ~300 Hz was used for all measurements.

2.3. CW-EPR/[55]Mn-ENDOR Simulations. CW-EPR/[55]Mn-ENDOR spectra were simultaneously fit assuming an effective spin $S = 1/2$ ground state (see Theory (section 3.2)). Calculations assumed that all tensors were colinear. The same Spin Hamiltonian was used for both CW-EPR and [55]Mn-ENDOR spectra. The electron Zeeman term was treated exactly. The nuclear Zeeman and hyperfine terms were treated using second order perturbation theory. Spectral simulations were performed numerically using Scilab-4.4.1, an open source vector-based linear algebra package (www.scilab.org) and the easyspin

package[72] in MATLAB. A Gaussian profile was used to describe the excitation line width, with a fwhm (full width at half maximum) of 20 MHz.

2.4. Computational Details. All models considered in the present study were optimized without restrictions, both with Ca^{2+} and with Sr^{2+}, using the previously benchmarked BP86 density functional[73,74] and TZVP basis sets for all atoms.[75] The optimizations took advantage of the RI approximation with the auxiliary def2-TZV/J Coulomb fitting basis sets[76] as implemented in ORCA.[77] Increased integration grids (Grid4 in ORCA convention) and tight SCF convergence criteria were used throughout. Exchange coupling constants (J_{ij}) for all pairs of Mn centers were subsequently computed for each optimized model using the broken-symmetry DFT methodology (BS-DFT),[78−81] assuming the isotropic Heisenberg Hamiltonian (Supporting Information eq S1). The hybrid meta-GGA TPSSh functional[82] was used in this case, and the calculations employed the chain-of-spheres (RIJCOSX) approximation to exact exchange.[83] Additionally, the effect of scalar relativistic effects was tested for selected systems using the zero-order regular approximation (ZORA) in conjunction with appropriately contracted all-electron scalar relativistic (SARC) basis sets.[84−86] Inclusion of scalar relativistic effects was not found to alter the results to any significant extent and thus was not considered further in the present study. The application of the BS-DFT approach and the performance of the TPSSh functional for the calculation of exchange coupling constants in oligonuclear manganese systems has been extensively discussed, benchmarked, and calibrated in previous studies of manganese dimers,[87−89] trimers,[90] and tetramers.[57,91]

3. THEORY

3.1. The Spin Hamiltonian Formalism. Here we consider an exchange coupled Mn tetramer. The current assignment for the oxidation states of the four Mn ion when poised in the S_2 state is $Mn^{III}Mn^{IV}Mn^{IV}Mn^{IV}$.[47,65,92,93] This net oxidation state is assumed throughout the text. A basis set that describes the Mn-tetramer spin manifold can be built from the product of the eigenstates of the four interacting spins

$$|S_1 S_2 S_3 S_4 M_1 M_2 M_3 M_4 I_1 I_2 I_3 I_4 m_1 m_2 m_3 m_4\rangle \quad (1)$$

Here S_i refers to the electronic spin state of Mn_i, M_i refers to the electronic magnetic sublevel of Mn_i, I_i refers to the nuclear spin state of Mn_i, and m_i refers to the nuclear magnetic sublevel of Mn_i. S_i takes the value 2 for Mn^{III} and 3/2 for Mn^{IV}; M_i takes the values S_i, S_i-1, ..., 1-S_i, -S_i; I_i takes the value 5/2 for ^{55}Mn; and m_i takes the values $-I_i$, 1-I_i, ..., I_i-1, I_i.

The Spin Hamiltonian that describes the spin manifold of the Mn tetramer is

$$H = \sum_i \beta_e B_0 \cdot g_i \cdot S_i - \sum_i g_n \beta_n B_0 \cdot I_i + \sum_i S_i \cdot a_i \cdot I_i$$
$$+ \sum_i I_i \cdot q_i \cdot I_i + \sum_i S_i \cdot d_i \cdot S_i - \sum_{i<j} S_i \cdot J_{ij} \cdot S_j \quad (2)$$

It contains the following: i) an electronic Zeeman term for each Mn ion; ii) a nuclear Zeeman term for each ^{55}Mn nucleus; iii) a hyperfine term for each ^{55}Mn nucleus; iv) a quadrupole term for each ^{55}Mn nucleus; v) a fine structure term for each Mn ion; and vi) pairwise exchange terms for each Mn−Mn interaction.

3.2. An Effective Spin 1/2 Ground State. The tetranuclear-manganese cluster of the OEC $Mn_4O_XCa(Sr)$, presents a daunting theoretical exercise. A basis set that describes the entire spin manifold of the coupled four Mn ions requires 414720 vectors, too many to be readily handled by current numerical techniques. The problem can be greatly simplified by assuming all Mn−Mn couplings are large, i.e. within the strong exchange

limit. For this, the exchange interactions between the Mn ions have to be significantly larger than any other term of the Spin Hamiltonian. The resultant electronic spin states of the manifold are then adequately described by a single quantum number, the total spin (S_T). The 'multiline' EPR signal observed for the S_2 state of the OEC is derived from only one total spin state, the ground state of the spin manifold with total spin $S_T = 1/2$. The basis set that describes this subspace requires only 2592 vectors which represent the coupling of the effective electronic spin ($S_T = 1/2$) to the nuclear spin of each Mn ($I = 5/2$) nucleus

$$\left| \frac{1}{2} \; M m_1 m_2 m_3 m_4 \right> \quad (3)$$

Where M takes all half-integer values: $-1/2 \leq M \leq 1/2$; and m_i (where $i = 1-4$) takes all half integer values: $-5/2 \leq m_i \leq 5/2$.

The effective Spin Hamiltonian that describes the ground state of the spin manifold ($S_T = 1/2$) is

$$H = \beta_e B_0 \cdot G \cdot S + \sum_i (g_n \beta_n B_0 \cdot I_i + S \cdot A_i \cdot I_i) \quad (4)$$

It contains the following: i) the Zeeman term for the total electronic spin; ii) Zeeman terms for each ^{55}Mn nucleus; and iii) hyperfine terms for each ^{55}Mn nucleus. Quadrupole terms are neglected as they are considered to only have a small contribution to the energy levels/eigenstates of the system. A description of the connection between the two Spin Hamiltonians given above is outlined in the Supporting Information S1 and S2.

4. RESULTS

4.1. CW-EPR/ESE-Detected Field Sweep Pulse EPR. CW-EPR spectra of the Mn_4O_XCa and Mn_4O_XSr OEC poised in the S_2 state are shown in Figure 2A. In both samples a point mutation was made to replace the tyrosine Y_D (D_2-Y_{160}) with a phenylalanine.[70] This mutation removed from the spectrum the $Y_D^\bullet$ (oxidized, radical form of Y_D) signal, which in *wild type* (*wt*) samples appears as a strong, narrow (fwhm ∼3 mT) signal centered at g ∼ 2 superimposing the central hyperfine lines of the S_2 state multiline signal.

The Mn_4O_XCa S_2 multiline signal reported here is very similar to previous literature reports.[67,68,94−98] The signal is centered about g∼2.0, and its hyperfine pattern contains at least 22 peaks, spread over the 250−430 mT field range.[99] A 'modified multiline' signal is observed for the Mn_4O_XSr OEC, poised in the S_2 state. The 'modified multiline' is also centered at about g∼2.0, and its hyperfine pattern is spread over the same field range (250−430 mT). The hyperfine pattern of the modified multiline resolves additional peaks compared to the Ca-multiline signal, so that a total of at least 24 peaks are observed with a markedly different line-intensity distribution. The modified multiline signal reported here is very similar to the Mn_4O_XSr multiline signal seen in higher plant (spinach) BBY type preparations obtained by chemical Ca^{2+}/Sr^{2+} exchange[26] and to an earlier study performed with *T. elongatus* grown photoautotrophically in Sr^{2+}-containing medium.[94]

Similar observations are seen for the pseudomodulated field sweep Q-band measurements obtained with *T. elongatus* samples containing $Y_D^\bullet$ (Figure 2B). The multiline signals are both centered at approximately g ∼ 2.0 and are spread over the same spectral range (1130−1320 mT). As at X-band, the Mn_4O_xSr OEC multiline does show more resolved hyperfine structure.

3638

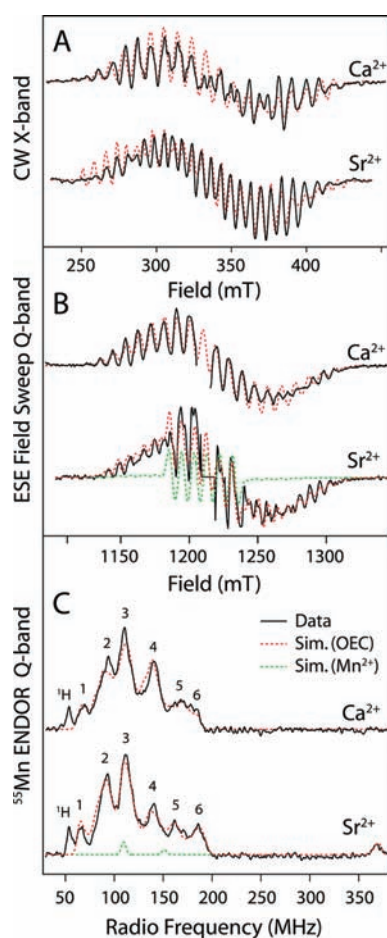dx.doi.org/10.1021/ja110145v |*J. Am. Chem. Soc.* 2011, 133, 3635–3648

Figure 2. EPR/ENDOR spectra of the Ca^{2+} and Sr^{2+} containing OEC, poised in the S_2 state, of PS II derived from *T. elongatus* (solid black lines). A) CW X-band. In these samples a point mutation was made to replace the tyrosine Y_D with a phenylalanine (Y160F). $Y_D^\bullet$ (oxidized, radical form) appears in wild type samples as a strong, narrow (fwhm ~3 mT) signal centered at g~2. Experimental parameters: microwave frequencies: 9.4097 GHz (Ca), 9.4213 GHz (Sr); microwave power: 20 mW; modulation amplitude: 25 G; time constant: 80 ms, temperature: 8.6 K. B) Q-band pulse EPR, ESE-detected field sweep. The derivative spectra represent the pseudo modulated (2 mT) raw data. The $Y_D^\bullet$, centered at about g ~ 2, was removed for clarity of presentation. Experimental parameters: microwave frequencies: 33.6870 GHz (Ca), 33.8160 GHz (Sr); shot repetition rate: 5 μs; microwave pulse length (π): 80 ns, τ: 440 ns, temperature: 4.2 K . C) Q-band pulse ^{55}Mn-Davies ENDOR. Spectra presented were smoothed using a 5 point moving average. Experimental parameters: microwave frequencies: 34.0450 GHz (Ca), 34.0286 GHz (Sr); magnetic field: B_0 = 1260 mT; shot repetition rate: 5 ms; microwave pulse length (π): 80 ns, τ: 440 ns, RF pulse (π_{RF}): 3.5 μs. The red dashed lines superimposing each trace represent a least-squares fitting to the whole data set using a model based on the Spin Hamiltonian formalism (see Theory eq 4). The optimized parameter sets are given in Table 1. It is noted that the Sr-OEC sample contains a small contribution of free Mn^{2+}. Mn^{2+} in protein environments and in solution appears as a narrow EPR signal centered at g~2, with 6 sharp peaks with peak-to-peak separation of 8–10 mT. In the corresponding ^{55}Mn-ENDOR experiment, three peaks are observed using the experimental conditions described above. These peaks are centered at the positions: 114, 158, and 375 MHz. The contribution of the Mn^{2+} signal is shown by the green dashed traces and is included in the OEC simulation profile shown by the red dashed traces. Simulation parameters for the Mn^{2+} artifact are given in the Supporting Information S3.
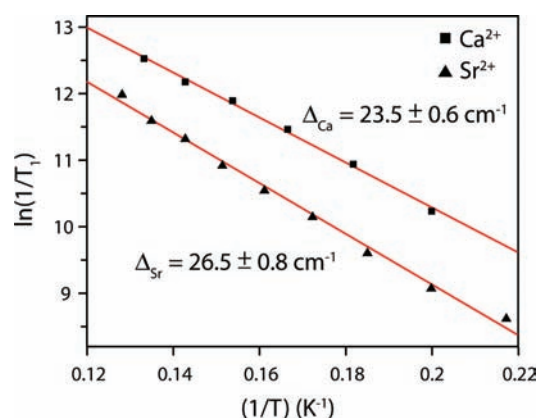

Figure 3. The temperature dependence of the T_1 relaxation time of the Ca^{2+} (■) and Sr^{2+} (▲) containing OEC in *T. elongatus*. The data are shown as the natural logarithm of the inverse of the T_1 time versus the inverse of the temperature. Electron spin echo-detected T_1 relaxation data were measured using a 3 pulse sequence: $\pi-\Delta T-\pi/2-\tau-\pi-\tau-$echo, where π = 80 ns, τ = 440 ns, and ΔT was swept over the range 0.1–10 ms. An estimate of the T_1 time was made by fitting the raw data to a biexponential decay collected at each temperature (see the Supporting Information). The superimposed red lines correspond to a linear fit of the data. The slope of each line is given in cm^{-1}. Both experiments were performed at B_0 = 1260 mT.

Q-band pulse spectroscopy is particularly sensitive to Mn^{2+}, and consequently a weak six-line Mn^{2+} signal is seen in the Q-band EPR spectrum of the Sr-PSII sample, which was not detectable in the corresponding X-band spectrum. The Mn^{2+} signal represents only a small fraction (<5%) of the PSII centers. It is not observed in the respective Ca^{2+} sample.

4.2. T_1 Relaxation of the Ca^{2+}/Sr^{2+} Containing OEC. Previous studies of higher plant *spinach* PS II[66,100] demonstrated that the OEC cluster in both the S_2 and S_0 oxidation states dominantly displays Orbach relaxation over the 5–10 K temperature range. As the relaxation rate of an Orbach process is dependent on the ground to first excited state energy separation, an estimate could be made for the energy ladder. Lorigan et al.[66] reported a ground to first excited state energy difference (Δ) of 35 cm^{-1} for the S_2 state, and Kulik et al.[100] reported Δ = 21.7 cm^{-1} for the S_0 state. Our measurements for S_2 in the cyanobacterium *T. elongatus* yielded very similar results (Figure 3). The Mn_4O_XCa and Mn_4O_XSr OEC poised in the S_2 state show Δ = 23.5 ± 0.6 cm^{-1} (31.0 K^{-1}) and Δ = 26.5 ± 0.8 cm^{-1} (35.8 K^{-1}), respectively. These results suggest that the energy ladder and thus the Mn electronic structure of the OEC with either Ca^{2+} or Sr^{2+} present are likely to be very similar in *T. elongatus*. The relatively large energy separation between the ground and first excited state allows us to consider the system as an effective spin 1/2 state, well removed from spin states of higher spin multiplicity (see Theory 3.2). Mn^{III} and Mn^{IV} typically have zero-field splittings (ZFS) of the order of $|\sim2$ cm$^{-1}|$ and $|\sim0.1$ cm$^{-1}|$, respectively (see Supporting Information S4). Similarly, the Zeeman term at Q-band is of the order of 1 cm^{-1}. Thus the exchange terms (J_{ij}) of the Spin Hamiltonian (eq 2) dominate the total zero-field splitting of the cluster. This allows us to treat the system in the strong exchange limit. It is noted though that this is only an approximation. The onsite ZFS of the individual Mn ions will effect the electronic structure, see Discussion.

4.3. ^{55}Mn-ENDOR. Figure 2C displays Q-band ^{55}Mn-Davies ENDOR spectra of the Mn_4O_xCa and Mn_4O_xSr OEC, poised in

the S_2-state measured at $B_0 = 1260$ mT. The line shape of the [55]Mn-ENDOR signal shows only a small field dependence over the 1190−1260 mT range, consistent with its assignment to the tetramanganese cluster[64,65] (see above). The Mn_4O_xCa spectrum shown in Figure 2C is similar but not identical to that reported in the previous study of Pudollek et al.;[101] the total ENDOR signal spans approximately the same width, but there are differences in the intensities of the individual lines. The spectra reported in Figure 2C were measured at a field position where the contribution from free or nonspecifically bound Mn^{2+} is small. Mn^{2+} signals of this type usually yield two relatively sharp lines at ∼115 MHz and ∼155 MHz and a third broader line at 375 MHz at all field positions across the 1190−1220 mT range. Control experiments on purposely denatured PSII samples clearly show these signals (see Figure S3 in the Supporting Information).

In contrast to the CW-X-band and field sweep ESE Q-band spectra (see Figures 2 and 3), the Mn_4O_XCa and Mn_4O_XSr OEC give rise to surprisingly similar [55]Mn-ENDOR spectra. No large difference is seen with regard to the total spectral breadth of the signal (60−200 MHz). The low field peak centered at ∼52 MHz originates from the magnetic coupling of protons with the Mn cluster. Approximately six peaks are resolved for both the Ca^{2+} and Sr^{2+} containing OEC. Small changes in the line-intensity of the six peaks are observed upon Ca^{2+}/Sr^{2+} replacement. It also appears that the maxima of peaks 1 and 2 downshift by approximately 10 MHz. The high frequency region clearly resolves two peaks in the Sr-containing OEC and peak 6 may upshift by ∼5 MHz as compared to Ca^{2+}. A comparison of the [55]Mn-ENDOR *T elongatus* data reported here with earlier higher plant spinach data[63,64,67] suggests that intrinsic differences between the two species are significantly larger than the effect of Ca^{2+}/Sr^{2+} replacement. The total spectral breadth of the [55]Mn-ENDOR spectrum is significantly larger in *T. elongatus* as compared to spinach.[64,65] The high frequency edge is approximately 20 MHz up-shifted, and the low frequency edge decreases by approximately the same degree.

4.4. Spectral Simulations of the EPR/ENDOR data. Spectral simulations of the EPR and ENDOR spectra of the Mn_4O_xCa and Mn_4O_xSr OEC poised in the S_2 state are described in the Materials and Methods and Theory section. CW X-band EPR (9 GHz), pulse Q-band EPR (34 GHz), and Q-band [55]Mn-ENDOR data were simultaneously fit using a least-squares routine. Powder pattern simulations are shown in Figure 2 as red dashed lines. The simulations reported here reproduce the total spectral breadth of the X- and Q-band multiline EPR signals for both the Mn_4O_XCa and Mn_4O_XSr and all the major spectral lines.

The fitted G and hyperfine tensors (A_i) are given in Table 1. Four hyperfine tensors are required to fit the EPR absorption and first derivative lineshapes at X- and Q-band (Figure 2A, B). Near axial symmetry was obtained for the fitted hyperfine tensors in the Mn_4O_xCa simulation. With the exception of A_1, the z component of all hyperfine tensors was the largest. The geometry and magnitude of the four hyperfine tensors are approximately the same as those determined in previous higher plant [55]Mn-ENDOR studies.[65,67] Comparison of the fitted parameters obtained for the Mn_4O_xCa and Mn_4O_xSr demonstrate that only small changes occur upon Ca^{2+}/Sr^{2+} replacement. Importantly, the four isotropic values ($A_{i,iso}$) of the fitted hyperfine tensors (Table 1) all approximately match for both OECs (<10% deviation) suggesting that there is no significant change in the electronic structure/coupling scheme of the Mn_4O_xCa/Sr

Table 1. Principal Values of the Effective G and [55]Mn HFI Tensors for the Simulations of the S_2 Spectra of Mn_4O_xCa and Mn_4O_xSr OEC from *T. elongatus*[a]

| | | G | A_i (MHz) | | | |
			A_1	A_2	A_3	A_4
Ca^{2+}	x	1.971	350	249	202	148
	y	1.948	310	227	182	162
	⊥	1.960	330	238	192	155
	z (‖)	1.985	275	278	240	263
	iso	1.968	312	251	208	191
	aniso	0.025	55	−40	−48	−108
Sr^{2+}	x	1.995	343	244	200	156
	y	1.968	361	217	185	152
	⊥	1.982	352	231	193	154
	z (‖)	1.957	293	268	223	210
	iso	1.973	332	243	203	173
	aniso	−0.025	59	−37	−30	−56

[a] The G-tensor principal values for the simulation of the S_2 spectra from Mn_4O_XCa OEC and Mn_4O_XCa were only allowed to vary by <0.05 compared to the values reported in ref 102. The isotropic G and A_i (i = 1-4) values are the average of the individual values: $G_{iso} = (G_x + G_y + G_z)/3$ and $A_{i,iso} = (A_{i,x} + A_{i,y} + A_{i,z})/3$. The equatorial and axial G and A_i values are defined as $G_\perp = (G_x + G_y)/3$, $G_\parallel = G_z$, and $A_{i\perp} = (A_{i,x} + A_{i,y})/2$, $A_{i\parallel} = A_{i,z}$. The anisotropy in the G and A_i values is expressed as the difference between the axial and equatorial component of the tensor.

Table 2. Experimental Spin Projections (ρ_i) for the Four Mn Centers As Estimated from the Fitted A_{iso} Values Listed in Table 1[a]

	Mn_1 (ρ_{iso1} Mn^{III})	Mn_2 (ρ_{iso2} Mn^{IV})	Mn_3 (ρ_{iso3} Mn^{IV})	Mn_4 (ρ_{iso4} Mn^{IV})
Ca^2	1.39−1.89	0.99−1.34	0.82−1.11	0.75−1.02
Sr^{2+}	1.48−2.01	0.96−1.30	0.80−1.09	0.68−0.93

[a] The ranges given result from the spread of the intrinsic isotropic hyperfine values reported in the literature for Mn^{III} and Mn^{IV} ions (Mn^{III}: $|a_{iso}| = 165$-225 MHz; Mn^{IV}: $|a_{iso}| = 187$-253 MHz; see Table S3 in the SI).

cluster. Instead, the change that occurs upon Ca^{2+}/Sr^{2+} substitution seems to manifest itself in a decrease in hyperfine tensor anisotropy e.g. see A_3 and A_4.

The principal values of the G-tensor were allowed to vary slightly (<± 0.05) from that reported by Teutloff et al.,[102] as deduced from high field measurements (W-band) on PSII crystals. As seen for the fitted hyperfine tensors, the isotropic G_{iso} value for the Mn_4O_XCa and Mn_4O_XSr OEC is approximately the same. It is again the anisotropy of the two clusters that is perturbed when Ca^{2+} is replaced by Sr^{2+}.

4.5. Experimental Spin Projections. The projection of the total spin onto each individual Mn ion was calculated as described in the Supporting Information S1 and S2. The obtained spin projection coefficients can be considered as a measure of the contribution of each Mn to the electronic structure; a measure of the electron density on each Mn ion. Spin projections (ρ_i) for each Mn were calculated by assuming: (i) the net oxidation state of S_2 was $Mn^{III}(Mn^{IV})_3$[47,65,92,93,103,104] and (ii) that the effective hyperfine tensor with the largest isotropic component was associated with the only Mn^{III} in the

3640

dx.doi.org/10.1021/ja110145v |*J. Am. Chem. Soc.* 2011, 133, 3635–3648

Table 3. Comparison of Ca^{2+}/Sr^{2+}−Mn and Mn−Mn Distances (Å) for the Optimized Calcium- and Strontium-Containing OEC Models (See Figure 1A-F), in the S$_2$ State (IV, IV, IV, III)^b

model	Ca/Sr−Mn$_A$	Ca/Sr -Mn$_B$	Ca/Sr -Mn$_C$	Ca/Sr -Mn$_D$	Mn$_A$-Mn$_B$	Mn$_B$-Mn$_C$	Mn$_C$-Mn$_D$	Mn$_B$-Mn$_D$
A-Ca^a	3.577	3.766	3.755	3.366	3.857	2.796	2.805	2.819
A-Sr	3.610	3.802	3.796	3.400	3.862	2.798	2.805	2.820
C-Ca	4.307	3.456	5.614	4.164	2.729	2.760	2.793	3.239
C-Sr	4.397	3.531	5.691	4.231	2.728	2.763	2.792	3.231
D-Ca	3.690	3.676	4.117	3.780	2.739	2.835	2.820	3.330
D-Sr	3.748	3.743	4.108	3.868	2.724	2.833	2.817	3.334
E-Ca	4.095	3.647	3.548	3.494	2.744	2.780	2.752	3.513
E-Sr	4.152	3.685	3.564	3.580	2.746	2.785	2.756	3.510
F-Ca	3.462	3.569	3.482	3.842	2.708	2.782	2.786	3.293
F-Sr	3.518	3.611	3.535	3.902	2.713	2.786	2.787	3.303

^{a} Mn$_A$−Mn$_C$ distances for model A are 3.680 Å and 3.683 Å for Ca and Sr, respectively. ^{b} The labels of the Mn atoms follow Figure 1, i.e. Mn$_A$, Mn$_B$ etc.

complex. The spin center of highest multiplicity (most unpaired electrons) is expected to carry the largest spin projection. This was indirectly tested for tetranuclear Mn complexes in the recent DFT study of Pantazis et al.[57] The experimental spin projections could then be calculated by simply taking the ratio of the isotropic component of the effective hyperfine tensors (A_1 to A_4) and literature values for the intrinsic isotropic hyperfine coupling seen in monomeric Mn^{III} and Mn^{IV} complexes[67,96,105−107] (see eq S4 in the Supporting Information S1 and S4). It is readily seen that the experimental spin projections for the Mn$_4$O$_X$Ca and Mn$_4$O$_X$Sr in *T. elongatus* for all four Mn ions are very similar. Only subtle changes are observed; the range of spin projection values of the Mn^{III} (associated with the hyperfine tensor A_1) upshift and one Mn^{IV} (associated with the hyperfine A_4) downshift for the Mn$_4$O$_X$Sr OEC relative to the Mn$_4$O$_X$Ca.

4.6. DFT Calculations. DFT calculations were performed on all OEC models (S$_2$ state) with published coordinates (see Figure 1) to assess the effect of Ca/Sr substitution on the electronic structure of the OEC. It must be stressed from the outset that our purpose here is not to evaluate these models as candidates for the OEC or to propose improvements based on their computed structural or spectroscopic properties but strictly to identify the differences —if any— between calcium-containing and strontium-containing systems. The respective Ca^{2+} and Sr^{2+} models were fully geometry optimized, i.e. without any constraints to the inorganic core or the movement of ligating amino acids, and subsequently their electronic structure was determined employing the methods described previously.[56,57] Accordingly, the differences observed between Ca^{2+}-containing and Sr^{2+}-containing structures of each model should be treated as upper-bound limits, in the sense that the protein backbone in the actual system can only be more restricted in its ability to adjust to ions of different size.

The structural variations observed upon substitution of Sr^{2+} for Ca^{2+} are uniform across all the various models considered, with differences in the optimized parameters being of the same nature and magnitude. Specifically, compared to the Ca^{2+} models, all optimized Sr−Mn distances are of the order of 0.06 Å longer compared to the corresponding Ca−Mn distances, giving the impression that the larger Sr^{2+} ion moves marginally "away" from the Mn$_4$O$_x$ cluster (Table 3). These uniform changes are readily attributed to the difference in ionic radius between calcium (0.99 Å) and strontium (1.12 Å).[108] The same observation was made in the polarized EXAFS study of Pushkar et al.[35] Most significant for the present study is that in the

Table 4. Comparison of Exchange Coupling Constants (cm^{-1}) between the Mn Sites (Mn$_A$, Mn$_B$, Mn$_C$, Mn$_D$) for Ca^{2+} and Sr^{2+}-Containing Models (See Figure 1A-F)

J	Mn$_A$-Mn$_B$	Mn$_A$-Mn$_C$	Mn$_A$-Mn$_D$	Mn$_B$-Mn$_C$	Mn$_B$-Mn$_D$	Mn$_C$-Mn$_D$
A-Ca	12	−13	0	57	20	46
A-Sr	11	−14	0	53	15	40
C-Ca	−90	8	0	−52	32	−81
C-Sr	−91	8	0	−55	31	−85
D-Ca	2	3	−4	−17	28	10
D-Sr	−1	3	−4	−17	28	9
E-Ca	1	4	−1	47	11	−80
E-Sr	−2	4	−1	39	12	−83
F-Ca	22	5	16	45	11	−43
F-Sr	16	6	15	37	11	−44

strontium-containing models the Mn−Mn and Mn−O distances remain essentially identical to those of the respective calcium-containing ones. Therefore, the present calculations confirm that the substitution of Ca^{2+} for Sr^{2+} does not affect the overall geometry of the Mn$_4$O$_x$ cluster, regardless of the particular topology assumed.

The above observations also imply that the exchange pathways regulating the magnetic coupling between the metal centers should not be very sensitive to the substitution, and this is indeed confirmed by the computed exchange coupling constants. From the results presented in Table 4 it is readily seen that there are practically no changes in most pairwise exchange interactions, consistent with the EPR/ENDOR results presented above. Regardless of the specific core topology, only minimal shifts are to be expected in the energy levels of the spin ladder.

According to the computed exchange coupling constants (see Table 4) two of the models (C and D) yield an $S = 1/2$ ground state; an $S = 5/2$ ground state is obtained for model E, whereas models A and F are predicted to have $S = 7/2$ ground spin states. Note however, that very small structural perturbations to model F can confer this model a $S = 1/2$ ground state, as shown for a backbone constrained version of the model used in ref 57, model 11 in that study.

A final note concerns the ^{55}Mn isotropic hyperfine coupling constants (A_{iso}), which can be computed for the present OEC models that display an $S = 1/2$ ground state after unconstrained optimization (models C and D). In line with the minimal perturbations on the exchange coupling interactions, the strontium-containing systems exhibit ^{55}Mn A_{iso} values that are almost identical with those of the calcium-containing systems. Specifically, for model C the computed A_{iso} values for centers Mn_A to Mn_D change from −212, −286, −262, and −413 MHz for the calcium system to −211, −284, −261, and −415 MHz for the strontium system. Similarly, the corresponding A_{iso} values for model D change from −227, −288, −191, and −449 MHz for the calcium system to −227, −287, −190, and −451 MHz for the strontium system, respectively. We consider these minute differences to be at the limit or beyond the expected accuracy of the present theoretical methodology. These results lend additional support to the hypothesis that strontium substitution does not lead to any significant change in the electronic structure of the OEC and to the overall spin density distribution.

5. DISCUSSION

5.1. General Considerations. Historically the 'modified multiline' observed upon Ca^{2+} substitution with Sr^{2+} has been thought to indicate a significant change of the electronic structure of the OEC. The data presented here requires a reappraisal of this hypothesis. The Mn_4O_XSr OEC of *T. elongatus*, which exhibits the same 'modified multiline spectra' seen in earlier studies performed on spinach preparations, displays very similar relaxation behavior and ^{55}Mn-ENDOR data as compared to the native Mn_4O_XCa OEC. This suggests a near equivalence of the electronic structures of the OEC when either Ca^{2+} or Sr^{2+} is present and thus supports the assignment of a functional instead of a structural role for Ca^{2+} in water splitting catalysis, such as substrate water binding/delivery, for reviews see ref 109.

5.2. Fitted Spin Hamiltonian Parameters. The reasonably good simulation quality observed for the fitting of the CW EPR X-band, pulse EPR Q-band, and Q-band ^{55}Mn-ENDOR spectra for both the Mn_4O_XCa and Mn_4O_XSr poised in the S_2 state demonstrates that the effective spin Hamiltonian approach outlined in the Theory section is sound. This result is consistent with the proposed energy-level scheme as determined by T_1 relaxation data. It supports the notion that the ground (doublet) state is well resolved (separated) from states of higher spin multiplicity. The inclusion of two microwave frequencies demonstrates that the correct estimates are made for both the field dependent (Zeeman) and field independent (Hyperfine) terms and shows that the zero-field splitting of each of the Mn ions needs not to be explicitly considered in order to simulate the EPR spectra. Similarly, the approximation that collinear tensors can be assumed for all Mn ions appears reasonable. In Mn dimer complexes, the same approximation holds due to the enforced symmetry of the μ-oxo-bridge motif.[96,105] As this is a key structural feature of the OEC,[6,7,47] it is not surprising that the same simplification can be applied. These general results are in line with previous simulation studies of Peloquin et al.,[67] Charlot et al.,[110] Kulik et al.,[65] Kusunoki and co-workers,[55,111] and Zheng et al.[106]

The changes that occur to the CW EPR and ^{55}Mn-ENDOR spectra upon Ca^{2+} replacement with Sr^{2+} can be rationalized by relatively small alterations in the effective hyperfine tensors. Only small changes are observed in the isotropic components of the
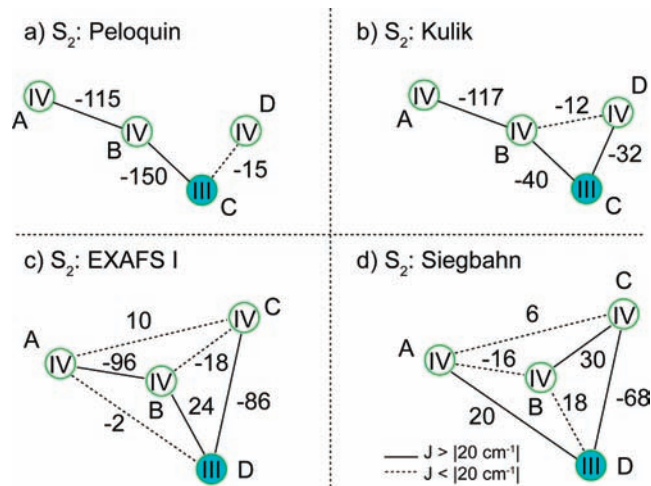

Figure 4. Current models for the electronic structure of the OEC in the S_2 state. a) The original model of Peloquin et al.;[67] b) Kulik model (Mn_C is the only Mn^{III} ion);[65] c) Pantazis model 1,[57] based on EXAFS core I;[6,57] and d) Pantazis model 11,[57] based on the Siegbahn structure.[11,58,59] The Peloquin, Kulik, and EXAFS I models require Mn_A to be strongly coupled to Mn_B. The Kulik, EXAFS I, and Siegbahn models require Mn_C to be strongly coupled to Mn_D. The EXAFS I and Siegbahn models differ by their connectivity of Mn_A to the trimer unit.

four hyperfine tensors. As, a consequence no significant change is seen for the onsite spin projection values, suggesting the electronic structure of the OEC (exchange pathways, distribution of oxidation states, etc.) is unaltered by Ca^{2+}/Sr^{2+} exchange. The same result is seen in our DFT calculations. Instead, the change that occurs upon Ca^{2+} substitution with Sr^{2+} appears to manifest itself in the fitted hyperfine tensor anisotropy.

5.3. Current Electronic Models of the OEC. Current models of the electronic structure of the OEC, which are developed from EPR/ENDOR studies, are all based on the '3 + 1' Mn tetramer topology, first proposed as possible geometric arrangement among other models by DeRose et al.[112] and as electronic models by Hasegawa et al.[111,113] and subsequently by Peloquin et al.[67] (Figure 4a). The Peloquin model was further refined by Charlot et al.,[110] Kulik et al.,[65] Britt et al.,[114] and Carrell et al.[115] A Y-shaped core was considered the most likely arrangement of the four Mn ions, where three of the Mn ions form a triangle unit (trimer), with the fourth Mn ion strongly coupled to one Mn ion of the triangle (Figure 4b). The position of the only Mn^{III} of the S_2 within the Y shaped core is ambiguous. Two consistent coupling schemes were developed by Kulik et al. where the Mn^{III} is assigned to either Mn_A or Mn_C. As stated in Kulik et al,[65] Mn_A was considered the most likely candidate for the Mn^{III} ion. This preference was based on the inferred changes in the exchange coupling scheme between the S_0 and S_2 oxidation states[65,116] and S_n state dependent changes in FTIR data.[117−119] This is in contrast to Charlot et al.[110] who instead favored assigning the Mn^{III} to one of the corners of the trimer (Mn_C or Mn_D). It is noted that in all models the Mn^{III} cannot be assigned to the connecting Mn_B, the corner of the triangle unit that makes the connection to the fourth outer Mn (Mn_A).

In our recent DFT study[57] we used the experimental electronic scheme discussed above, developed from higher plant EPR/ENDOR data, to screen all possible models for the state S_2 of the OEC (see Introduction) two coupling schemes based on the EXAFS core I[6] (Figure 1C) topology and the Siegbahn

3642

dx.doi.org/10.1021/ja110145v |*J. Am. Chem. Soc.* 2011, 133, 3635–3648

core[11,58,59] (Figure 1 F) were identified as promising candidates for the OEC. It is noted that the Siegbahn structure was slightly modified (as compared to the structure reported in ref[11]) to confer it a ground state of spin 1/2, see Pantazis et al.[57] The electronic coupling schemes for both models are shown in Figure 4 (c and d). These two models were selected as they (i) reproduce the correct ground state spin multiplicity ($S = 1/2$); (ii) the correct ground to first excited state energy difference (to within a factor of 2−3); and (iii) yield a spin projection coefficient of ~1 on all four Mn ions, consistent with the EPR/ENDOR data discussed in detail above. This is in contrast to the other models shown in Figure 1. DFT calculations for model A, based on the London structure, never reproduce a ground state $S = 1/2$, as seen for the S_2 multiline signal. Similarly, EXAFS models II and III (Figure 1 D, E), do not reproduce the correct ground to first excited state energy difference or spin projection coefficients. Model B has yet to be tested as coordinates for this model are not published.

The two preferred DFT developed exchange coupling schemes, denoted EXAFS I (Figure 1C) and Siegbahn (Figure 1F), broadly match the experimentally derived coupling scheme of Kulik et al., where Mn_C is the Mn^{III}. It is noted though that these two new models are more sophisticated, due to the inclusion of additional exchange pathways. As such, the three schemes: Kulik, EXAFS I, and Siegbahn (Figure 4 b, c, d) differ mainly in the electronic coupling of the outer Mn_A to the trimer (Mn_B, Mn_C, Mn_D) unit. The two DFT models (EXAFS I and Siegbahn) have the same Mn−O bridging pattern (see Scheme 1) but differ in the geometry around Mn_B and the ligation by amino acids. Nevertheless, they both require Mn_D to be the Mn^{III} ion, and that it has a square-pyramidal ligand field.[120] In the subsequent section we will show that the above Ca^{2+}/Sr^{2+} data obtained with *T. elongatus* core preparations provide a robust experimental test for these two models.

5.4. Ca^{2+}/Sr^{2+} Substitution − an Experimental Test of the Current Electronic Models of the OEC.
The large anisotropy seen for the fitted hyperfine tensors (A_2-A_4; Table 1) of both the Ca^{2+} and the Sr^{2+} OEC is outside the range seen for monomeric model Mn^{IV} complexes (see Supporting Information S4). A similar observation was previously made for dimeric mixed valence $Mn^{III}Mn^{IV}$ model complexes.[67,105,107,121] This phenomenon was interpreted as the 'transfer of anisotropy' from the Mn^{III} to the Mn^{IV}. More accurately though it represents a partial breakdown of the simple description of the spin system in terms of an effective spin 1/2 ground state. As outlined above (see Theory and Supporting Information S1) this description requires the ZFS of the whole cluster (i.e., exchange couplings between the four Mn) to be significantly larger than any other term of the Spin Hamiltonian. As can be seen from the coupling schemes displayed in Figure 4 this is, despite the overall good fit quality achieved with this approach, not strictly the case, as the onsite ZFS of the Mn^{III}, typically ~1−3 cm^{-1}, is of the similar order as some Mn−Mn exchange couplings (i.e., ~10 cm^{-1}). It is noted that in octahedral ligand environments the inherent symmetry of the Mn^{IV}'s half filled $^3T_{2g}$ levels usually leads to small zero-field splittings ($|d| < 0.1$ cm^{-1}).[107]

The effect of the onsite ZFS of the Mn^{III} ion can be taken into account in the calculation of the spin projections (see Supporting Information S1). Here, the spin projections for all four Mn ions have to be considered as tensors as opposed to scalar quantities; their magnitude is now orientationally dependent. As the Mn^{III} ion is strongly exchange coupled to the three Mn^{IV} ions, the inclusion of the intrinsic ZFS of the Mn^{III} does not only influence

the spin projection of Mn^{III} but of all four Mn ions. Thus the fitted hyperfine tensor anisotropy for the three Mn^{IV} ions in Table 1 is a measure of the onsite ZFS of the Mn^{III}. Based on this interpretation, a change in the tensor anisotropy of the hyperfine tensors between the Ca^{2+} and Sr^{2+} OECs indicates that Ca^{2+}/Sr^{2+} exchange alters the onsite ZFS of the only Mn^{III} of the OEC in the S_2 state. That is to say, Ca^{2+}/Sr^{2+} exchange perturbs the ligand environment of the Mn^{III} ion.

It is suggested that this provides a means to test the current electronic models of the OEC. From the previous sections it was shown that (i) there is virtually no change in the electronic coupling pathways (J_{ij}) when Ca^{2+} is replaced by Sr^{2+}, as the isotropic spin projections on all four Mn are very similar and (ii) there is no large structural change that occurs when Ca^{2+} is replaced by Sr^{2+}, i.e. the coordination of the Mn^{III} does not change. Within this framework we would expect that for an electronic model to be consistent it should give (i) sensible onsite ZFS values for both the Ca^{2+} and Sr^{2+} OECs. Here we will define 'sensible' as within the range of ZFS measured in monomeric Mn^{III} model complexes i.e. $1 < |d| < 5$ cm^{-1} (see Supporting Information S4); and (ii) we would expect that the change of the onsite ZFS of the Mn^{III} that occurs when Ca^{2+} is replaced with Sr^{2+} would be small ($< |1|$ cm^{-1}). Typically, Mn^{III} complexes of the same type/coordination environment (e.g., porphyrins, corroles, etc.) give similar ZFS values ($\ll |1|$ cm^{-1}). A quantitative assessment of the EXAFS I and Siegbahn model is presented in section 5.4.2.

Finally it is noted that the onsite ZFS of the Mn^{III} ion, in addition to changing the effective hyperfine tensors (A_i), will also perturb the effective G tensor of the system in an analogous way. Thus it is not surprising that in the fittings of the Mn_4O_XCa and Mn_4O_XSr EPR/ENDOR data, the isotropic G tensor component is approximately the same for the two systems while the anisotropic component changes. Furthermore, the contribution of the ZFS of the Mn^{III} to the G anisotropy will depend on the frequency at which the EPR measurement is performed. This leads to, in our simplified $S = 1/2$ fit approach, an apparent frequency dependence of the G anisotropy, which may explain why we observe good agreement in terms of the frequency independent isotropic component of the G tensor in our X- and Q-band simulations as compared to the high field measurements of Teuloff et al.,[102] but by contrast infer a different G anisotropy.

5.4.1. The Onsite Zero-Field Spitting (ZFS) of the Mn^{III}. The sign of the onsite ZFS of the Mn^{III} provides important information of its ligand environment. Mn^{III} ($S = 2$) is a d^4 ion, which does not usually exhibit Kramers degeneracy at zero-field.[107,122−124] The inherent asymmetry of the valence electron configuration leads to a large Jahn−Teller distortion, due to a coupling of the electronic and nuclear motion. Spin−orbit coupling removes the degeneracy of the ^5E_g energy-levels giving rise to either an $^5A_{1g}$ or $^5B_{1g}$ ground state.[122,125] It was demonstrated in refs 125 and 126 that

i) a $^5A_{1g}$ ground state is obtained for a trigonal bipyramidal (5-coordinate) or a tetragonally compressed octahedral (6-coordinate) ligand geometry (see Figure 5). The vacant electron orbital is the d_{z^2} orbital. Spectroscopically this manifests itself as both a positive ZFS parameter (d) and yields a positive hyperfine tensor anisotropy, where the anisotropy of the hyperfine tensor is defined as the difference between the absolute values of the axial and equatorial hyperfine components ($a_\Delta = |a_\parallel| - |a_\perp|$), for a complete discussion see Campbell et al.[126]

ii) a $^5B_{1g}$ ground state is obtained for a square-pyramidal (5-coordinate) or tetragonally elongated (6-coordinate) ligand geometry (see Figure 5). The vacant electron orbital is now
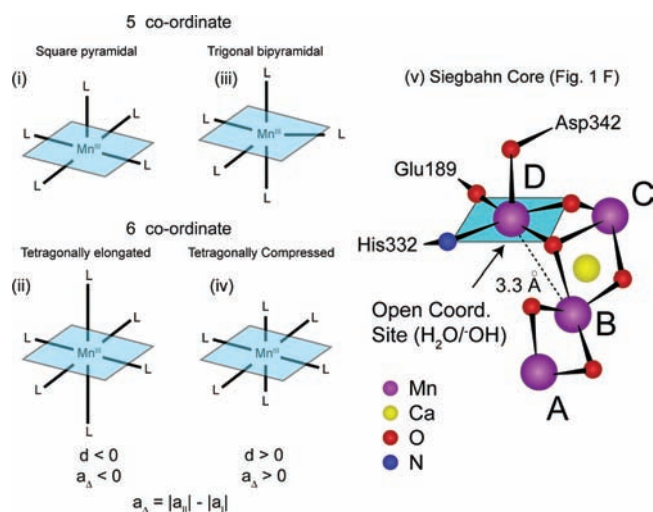
3643

dx.doi.org/10.1021/ja110145v |*J. Am. Chem. Soc.* 2011, 133, 3635–3648

Figure 5. The coordination environment of Mn^{III} and its correlation with the sign of d, the ZFS parameter. Mn^{III} complexes that exhibit a $^5B_{1g}$ ground state (left side, models i, ii) display a negative d value; the vacant d-orbital is $d_{x^2-y^2}$; and the ligand environment of the Mn^{III} is either: (i) 5-coordinate square planar or (ii) 6-coordinate tetragonally elongated. Mn^{III} complexes that exhibit a $^5A_{1g}$ ground state (center, models iii, iv) display a positive d value; the vacant d-orbital is d_{z^2}; and the ligand environment of the Mn^{III} is either: (iii) 5-coordinate trigonal bipyramidal or (iv) 6-coordinate tetragonally compressed. Right side (v): The ligand environment of the Mn^{III} in the Siegbahn core (Figure 1F).

the $d_{x^2-y^2}$ orbital. Spectroscopically this manifests itself as both a negative ZFS parameter (d) and yields a negative hyperfine tensor anisotropy as defined above.

This behavior was observed for monomeric Mn^{III} model complexes and mixed valence $Mn^{II}Mn^{III}$ and $Mn^{III}Mn^{IV}$ dimers (see Supporting Information S4). The only exception known is the complex *trans*-[Mn(cyclam)I$_2$]I,[127] which is thought to have unique, low-lying charge transfer states which strongly perturbs the ground state multiplet. Thus the sign of the onsite ZFS of the Mn^{III} (d) provides another criterion that we can use to test current OEC models. As both the EXAFS I and Siegbahn model contain a Mn^{III} that has 5 coordination, a square-pyramidal ligand field, the Mn^{III} onsite ZFS (d) value has to be negative for these models to be consistent.

5.4.2. The Onsite ZFS (d) of the Mn^{III} for the Two Selected DFT Models: EXAFS I and Siegbahn. Figure 6 displays a graphical analysis of the dependence of the spin projections and consequently the inferred onsite/intrinsic hyperfine tensors (a_i) of the individual Mn ions as a function of the Mn zero-field splitting of the Mn^{III} ion (d). The analysis presented in Figure 6 is based on the Siegbahn core exchange coupling scheme (Figure 1F and Figure 4d). A similar figure for EXAFS I model is given in the Supporting Information S5. Panel A displays the dependence of the axial and equatorial components of the spin projection tensor of each of the four Mn (A, B, C, D) ions as a function of the ZFS of the Mn^{III}. When $d = 0$, the two components are necessarily equal. It can be readily observed that the correct anisotropy of the effective hyperfine tensors of the Mn^{IV} ions can only be reproduced if the d value is negative. This yields a larger axial as opposed to equatorial spin projection component, as seen for the effective Mn^{IV} hyperfine tensors (A_2-A_4). It is noted that while the spin projections are signed quantities, the sign cannot be extracted from the effective hyperfine tensors. As such we are only interested in the absolute magnitude of the spin projection
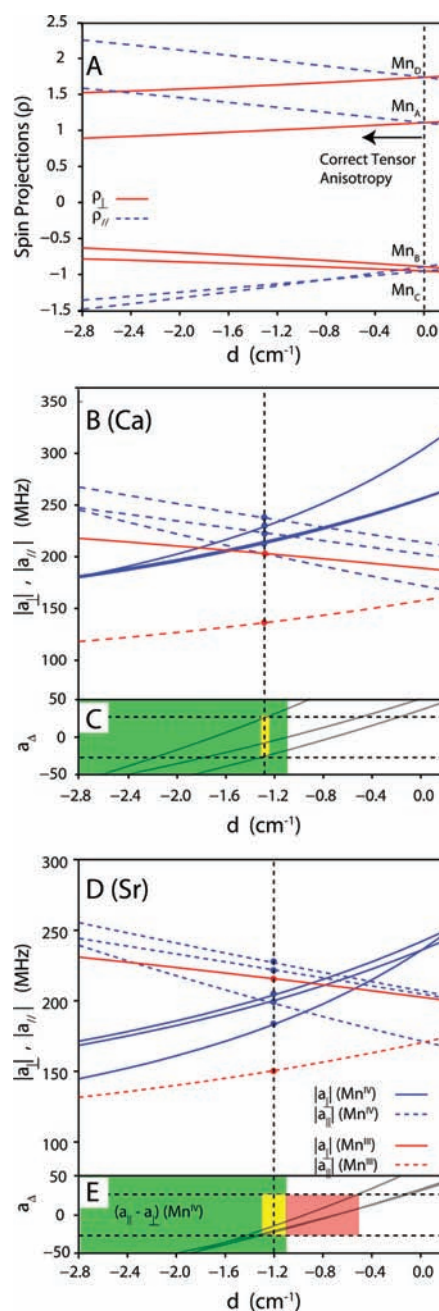

Figure 6. Panel A: The dependence of the spin projection factors ($\rho_\perp$, $\rho_\parallel$) on the zero-field splitting parameter (d) of the Mn^{III} ion assuming the exchange coupling model for the Siegbahn core (scheme Figure 1F). Panel B: The dependence of the on-site hyperfine tensor components ($a_\perp$, $a_\parallel$) of the Mn_4O_XCa cluster for each of the four manganese ions on the zero-field splitting parameter (d) of the Mn^{III} ion (see text). The bottom panel (C) shows the difference (a_Δ) between the parallel ($a_\parallel$ or a_Z) and perpendicular ($a_\perp$ or a_X, a_Y) hyperfine components of the three Mn^{IV} ions. The green shaded region represents the range of ZFS values for the Mn^{III} seen in model complexes (when $d < 0$). The red shaded region represents the range of acceptable ZFS values for the Mn^{III} which are consistent with the electronic model, i.e. the range over which the intrinsic hyperfine anisotropy of the Mn^{IV} ions are within the range seen for model complexes. Their intersection is shown by the yellow shaded region. Panels D and E are exactly the same as panels B and C, except that here the Sr-containing OEC was examined. Table 5 lists the intrinsic hyperfine tensor components for all four Mn ions calculated at the midpoint of the range of consistent d values i.e. the yellow shaded region.

Table 5. Calculated Spin Projection Tensor Components ($\rho_\perp$, $\rho_\parallel$) and Isotropic Hyperfine Tensor Components ($a_\perp$, $a_\parallel$) for the 4 Mn Ions of the OEC[a]

(i) Siegbahn core		$\rho_\perp$	$\rho_\parallel$	$a_\perp$	$a_\parallel$	a_{iso}	a_{aniso}
Ca^{2+}	Mn_A (Mn^{IV})	1.01	1.33	235.2	209.6	226.6	−25.6 (−8.5)
d (Mn^{III}) = −1.32 to −1.26 cm^{-1}	Mn_B (Mn^{IV})	−0.77	−1.16	201.7	226.7	210.0	25.0 (8.3)
d_{midpt} = −1.29 cm^{-1}	Mn_C (Mn^{IV})	−0.87	−1.12	221.6	213.5	218.9	−8.0 (−2.7)
	Mn_D (Mn^{III})	1.62	1.96	203.3	140.5	182.4	−62.8 (−20.9)
Sr^{2+}	Mn_A (Mn^{IV})	1.02	1.31	226.9	204.0	219.3	−22.9 (−7.6)
d (Mn^{III}) = −1.31 to −1.1 cm^{-1}	Mn_B (Mn^{IV})	−0.78	−1.14	198.5	183.6	193.5	−15.0 (−5.0)
d_{midpt} = −1.21 cm^{-1}	Mn_C (Mn^{IV})	−0.87	−1.11	221.5	200.4	214.5	−21.2 (−7.1)
	Mn_D (Mn^{III})	1.63	1.94	216.1	150.7	194.3	−65.3 (−21.8)
(ii) EXAFS I		$\rho_\perp$	$\rho_\parallel$	$a_\perp$	$a_\parallel$	a_{iso}	a_{aniso}
Ca^{2+}	Mn_A (Mn^{IV})	−0.75	−1.10	205.4	238.5	216.4	33.2 (11.1)
d (Mn^{III}) = −6.8 to −5.6 cm^{-1}	Mn_B (Mn^{IV})	0.93	1.22	255.2	227.5	246.0	−27.7 (−9.2)
d_{midpt} = −6.2 cm^{-1}	Mn_C (Mn^{IV})	−0.86	−1.27	222.7	189.2	211.5	−33.4 (−11.1)
	Mn_D (Mn^{III})	1.68	2.15	195.9	128.0	173.3	−67.9 (−22.6)
Sr^{2+}	Mn_A (Mn^{IV})	−0.80	−1.00	193.0	209.3	198.4	16.3 (5.4)
d (Mn^{III}) = −4.4 to −2.8 cm^{-1}	Mn_B (Mn^{IV})	0.97	1.14	238.5	235.2	237.4	−3.3 (−1.1)
d_{midpt} = −3.6 cm^{-1}	Mn_C (Mn^{IV})	−0.91	−1.15	211.4	193.7	205.5	−17.8 (−5.9)
	Mn_D (Mn^{III})	1.74	2.01	202.0	145.4	183.1	−56.7 (−18.9)

[a] The isotropic a_i values are defined as $a_{i,iso} = (2a_{i\perp} + a_{i\parallel})/3$. The anisotropy $a_{i,aniso}$ is expressed as the difference between the axial and equatorial component of the tensor. For direct comparison to the work of Peloquin et al.[67] the anisotropy is also expressed in terms of a_{aniso} described above, divided by three (see value in brackets).

components and not their signed magnitude. The onsite/intrinsic axial and equatorial hyperfine tensor components ($a_\parallel$, $a_\perp$) can be calculated from the spin projection components seen in panel A ($\rho_\parallel$, $\rho_\perp$), and the fitted effective hyperfine tensor components ($A_\parallel$, $A_\perp$) based on eq S4. Their dependence on the choice of the ZFS of the Mn^{III} ion is shown in Figure 6 panels B, C (Mn_4O_XCa) and panels D, E (Mn_4O_XSr).

(i) Siegbahn Core. The inferred ZFS of the Mn^{III} ion for the Siegbahn core is ~ -1.3 cm^{-1}, for the Ca^{2+} containing OEC. This value is small for a Mn^{III} ion, falling just inside the range of d values seen in model complexes i.e. $1 < |d| < 5$ cm^{-1} (see Supporting Information S4). The range of consistent ZFS values for the Mn^{III} in the Sr^{2+} containing OEC is broader and shifting to lower $|d|$. Intrinsic hyperfine parameters were calculated at the midpoint of the range of consistent d values, i.e. the yellow shaded region shown in Figure 6 (see figure caption) for both the Ca^{2+} and Sr^{2+} containing OEC (see Table 5). It is readily observed that only a small change in the d value (<0.1 cm^{-1}) of the Mn^{III} results in very similar intrinsic hyperfine tensors for all four Mn, i.e. the same intrinsic hyperfine parameters can be generated from the Ca^{2+} and Sr^{2+} EPR/ENDOR parameter sets by adjusting the ZFS of the Mn^{III} by <0.1 cm^{-1}. Thus the Siegbahn core is consistent with the two criteria described at the end of section 5.4: (i) the model gives sensible onsite ZFS values for both the Ca^{2+} and Sr^{2+} OECs and (ii) the change of the onsite ZFS of the Mn^{III} that occurs when Ca^{2+} is replaced with Sr^{2+} must be small.

It is also noted that the d value is negative and the intrinsic parameters for the Mn^{III} are as follows: $a_{iso} \sim 182$ MHz, $a_\perp \sim 203$ MHz, $a_\parallel \sim 1491$ MHz, $a_{aniso} \sim 63$ MHz. These values are consistent with a Mn^{III} with a square-pyramidal ligand field (see section 5.4.1), that is to say, with the co-ordination sphere seen for the Mn^{III} in the Siegbahn core (Figure 5v).

(ii) EXAFS Core I. Unlike the Siegbahn model, there is no consistent range for the ZFS for the Mn^{III} ion for the Ca^{2+}

containing OEC, i.e. there is no range of ZFS values for the Mn^{III} where the intrinsic hyperfine tensor anisotropy for all three Mn^{IV} hyperfine tensors are simultaneously within the range seen for model Mn^{IV} complexes, (see Supporting Information S4 and S5). Furthermore, if we consider the solution space just outside the range seen for model complexes, we find that the predicted range of ZFS for the Mn^{III} is very large, -6.8 cm^{-1} to -5.6 cm^{-1}. These values are outside the range seen for Mn^{III} model complexes. We also note that the inferred change in the ZFS of the Mn^{III} when Ca^{2+} is replaced by Sr^{2+} is also large, $\sim |2|$ cm^{-1} range. These observations do not fulfill the two criteria introduced in section 5.4 and thus suggest the EXAFS I model is inconsistent with the EPR/ENDOR data presented here, in its current construction.

Thus from the currently available DFT models with published coordinates only the Siegbahn model is found in our EPR/ENDOR analysis to be consistent with model complex data (see Supporting Information S4). This consistency between proposed structure and calculated and measured EPR/ENDOR parameters further supports the oxidation state model used in the above analysis, i.e. S_2 contains three Mn^{IV} and one Mn^{III} and that the assignment that Mn_D is the only Mn^{III} ion in the S_2 state. The above conclusions about the geometry of the Mn^{III} site also agrees with i) the original ^{55}Mn-ENDOR analysis of Peloquin et al., which was performed on higher plant spinach data employing the simpler coupling topology shown in Figure 4a, and ii) recent DFT calculations by Schinzel et al.[128]

5.5. The Physical Nature of the Ca/Sr Effect − The Near-Infrared Absorption Band. The Siegbahn core assigns the position of the only Mn^{III} in the S_2 state to within the distorted cuboidal Mn_3O_3Ca element; the Mn^{III} has a μ-oxo linkage to the Ca^{2+}/Sr^{2+} site. Experimental evidence from EXAFS suggests the Ca^{2+}/Sr^{2+} substitution leads to a small elongation of the Mn−Sr distance of the order of ~ 0.1 Å.[35] DFT calculations on the Siegbahn structure above, where the Ca was replaced by the Sr,

reproduced the same result; the Mn−Ca/Sr distance lengthens by 0.03−0.09 Å when Ca^{2+} is replaced by Sr^{2+}. Thus Sr substitution in this model should indeed modify the co-ordination sphere of the Mn^{III} ion. It is this change that could presumably lead to a decrease in the Mn^{III} zero-field splitting parameter d and, as shown above, consequently to the 'modified multiline' EPR signal.

Consistent with this interpretation is the known effect of Ca/Sr substitution on the sensitivity of the OEC to near-infrared (NIR) light. The native OEC poised in the S_2 state is sensitive to NIR light under certain conditions.[94,129] NIR can induce a conformational change that converts the $S_T = 1/2$ multiline state into a high spin species ($S_T \geq 5/2$), with a broad EPR resonance at $g = 4.1$ in spinach[129] and higher g-values in cyanobacteria preparations.[94] It is interesting to note that the spin state of the natural Mn_4O_xCa cluster is quite sensitive, and signals with $S_T = 1/2$, 5/2 and 7/2 have been observed depending on species, alcohol additions, and cryoprotectant conditions.[94,130−134] It is expected that the absorption characteristics of the NIR bands of the OEC in the S_2 state will be strongly dependent on the Mn^{III} ion; as Mn^{III} model complexes can exhibit strong d-d transitions in this wavelength region. Ca^{2+} substitution with Sr^{2+} enhances the sensitivity of the OEC toward NIR light, suggesting the Mn^{III} NIR absorption profile has been in some way perturbed. Changes of the ZFS of the Mn^{III} of the order of ~0.1 cm^{-1}, as inferred from our above EPR/ENDOR analysis could sufficiently shift the absorption(s) or change the extinction coefficient(s) of the Mn^{III} ion and thus explain the enhancement of the conversion of the multiline signal to the $g = 4.1$ signal in the S_2 state.

CONCLUSIONS

The multifrequency EPR and ENDOR analysis presented above demonstrates that Ca^{2+} replacement with Sr^{2+} does not significantly alter the overall electronic structure of the OEC. The spin density distribution across the tetramanganese cluster does not change significantly as estimated from the isotropic component of the four fitted hyperfine tensors. This result is consistent with structural data (EXAFS) which demonstrated that only small elongatations in Mn−Ca/Sr distances are observed in the Mn_4O_XSr cluster, and with DFT calculations presented here that show that Sr does not significantly alter Mn−Mn distances and the exchange coupling pathways of the Mn_4O_x complex. The effect of Ca/Sr substitution on the electronic structure of the OEC is interpreted as a small modification to the ZFS of the Mn^{III} ion, which is shown to have a 5-coordinate square-bipyramidal or 6-coordinate tetragonally elongated ligand field. The presented EPR/ENDOR data are consistent with only one current structural model of the OEC, namely the Siegbahn core. Within this model the only Mn^{III} of the S_2 state is structurally coupled to the Ca/Sr ion via a μ-oxo or μ-hydroxo bridge.

The Mn_4O_xCa core topology of the Siegbahn model is such that it contains, like EXAFS models I−III (Figure 1 C-E), three short Mn−Mn distances, and one long (3.3 Å) Mn−Mn distance. The long Mn−Mn distance is inside a distorted cuboidal structure and forms its open site. The missing 'corner oxygen' leads to a 5-coordinate, square-pyramidal ligation for the Mn_D^{III} ion in the S_2 state. Assuming that a substrate 'water' (H_2O, OH^-) binds to this open coordination site of Mn_D during the $S_2 \rightarrow S_3$ transition (either from bulk water or water bound to Ca^{2+}) or that it is already very weakly bound in the S_2 state (tetragonally elongated coordination site), the 3.3 Å

Mn−Mn distance could provide an ideal geometry for low energy barrier O−O bond formation during the $S_3 \rightarrow S_4 \rightarrow S_0$ transition.[11,56,65,135,136]

■ ASSOCIATED CONTENT

ⓢ Supporting Information. Additional material detailing spin projection calculations, collated data on model Mn^{III} and Mn^{IV} complexes, and additional graphs that show the effect of the ZFS of the Mn^{III} for all literature models with a spin 1/2 ground state. This material is available free of charge via the Internet at http://pubs.acs.org.

■ AUTHOR INFORMATION

Corresponding Author
*Phone: +49-208-306-3865. E-mail: cox@mpi-muelheim.mpg.de (N.C.). Phone: +46-90-7865933. E-mail: johannes.messinger@ chem.umu.se (J.M.). Phone: +49-208-306-3614. E-mail: lubitz@ mpi-muelheim.mpg.de (W.L.).

■ ACKNOWLEDGMENT

■ REFERENCES

(1) Zouni, A.; Witt, H.-T.; Kern, J.; Fromme, P.; Krauss, N.; Saenger, W.; Orth, P. *Nature* **2001**, *409*, 739–743.

(2) Kamiya, N.; Shen, J.-R. *Proc. Natl. Acad. Sci. U.S.A.* **2003**, *100*, 98–103.

(3) Ferreira, K. N.; Iverson, T. M.; Maghlaoui, K.; Barber, J.; Iwata, S. *Science* **2004**, *303*, 1831–1838.

(4) Loll, B.; Kern, J.; Saenger, W.; Zouni, A.; Biesiadka, J. *Nature* **2005**, *438*, 1040–1044.

(5) Guskov, A.; Kern, J.; Gabdulkhakov, A.; Broser, M.; Zouni, A.; Saenger, W. *Nat. Struct. Mol. Biol.* **2009**, *16*, 334–342.

(6) Yano, J.; Kern, J.; Sauer, K.; Latimer, M. J.; Pushkar, Y.; Biesiadka, J.; Loll, B.; Saenger, W.; Messinger, J.; Zouni, A.; Yachandra, V. K. *Science* **2006**, *314*, 821–825.

(7) Pushkar, Y.; Yano, J.; Glatzel, P.; Messinger, J.; Lewis, A.; Sauer, K.; Bergmann, U.; Yachandra, V. K. *J. Biol. Chem.* **2007**, *282*, 7198–7208.

(8) Lubitz, W.; Reijerse, E. J.; Messinger, J. *Energy Environ. Sci.* **2008**, *1*, 15–31.

(9) Messinger, J.; Renger, G. In *Primary Processes of Photosynthesis - Part 2: Basic Principles and Apparatus*; Renger, G., Ed.; Royal Society of Chemistry: Cambridge, 2008; pp 291−349.

(10) Hillier, W.; Messinger, J. *Mechanism of photosynthetic oxygen production*; Springer, 2005; Vol. 1.

(11) Siegbahn, P. E. M. *Acc. Chem. Res.* **2009**, *42*, 1871–1880.

(12) Dasgupta, J.; van Willigen, R. T.; Dismukes, G. C. *Phys. Chem. Chem. Phys.* **2004**, *6*, 4793–4802.

(13) Dau, H.; Zaharieva, I. *Acc. Chem. Res.* **2009**, *42*, 1861–1870.

(14) McEvoy, J. P.; Brudvig, G. W. *Chem. Rev.* **2006**, *106*, 4455–4483.

(15) Tommos, C.; Babcock, G. T. *Acc. Chem. Res.* **1998**, *31*, 18–25.

(16) Åhrling, K.; Pace, R. J.; Evans, M. C. W. *The catalytic Manganese Cluster: Implications from Spectroscopy*; Springer, 2005; Vol. 1.

(17) Nelson, N.; Yocum, C. F. *Annu. Rev. Plant Biol.* **2006**, *57*, 521–565.

(18) Renger, G.; Renger, T. *Photosynth. Res.* **2008**, *98*, 53–80.

(19) Kok, B.; Forbush, B.; McGloin, M. *Photochem. Photobiol.* **1970**, *11*, 457–475.

(20) Ono, T.-A.; Inoue, Y. *FEBS Lett.* **1988**, *227*, 147–152.

(21) Boussac, A.; Zimmermann, J. L.; Rutherford, A. W. *Biochemistry* **1989**, *28*, 8984–8989.

(22) Boussac, A.; Zimmermann, J.-L.; Rutherford, A. W. *FEBS Lett.* **1990**, *277*, 69–74.

(23) Ghanotakis, D. F.; Babcock, G. T.; Yocum, C. F. *FEBS Lett.* **1984**, *167*, 127–130.

(24) Sandusky, P. O.; Yocum, C. F. *Biochim. Biophys. Acta* **1984**, *766*, 603–611.

(25) Sandusky, P. O.; Yocum, C. F. *Biochim. Biophys. Acta* **1986**, *849*, 85–93.

(26) Boussac, A.; Rutherford, A. W. *Biochemistry* **1988**, *27*, 3476–3483.

(27) Boussac, A.; Rappaport, F.; Carrier, P.; Verbavatz, J. M.; Gobin, R.; Kirilovsky, D.; Rutherford, A. W.; Sugiura, M. *J. Biol. Chem.* **2004**, *279*, 22809–22819.

(28) Vrettos, J. S.; Stone, D. A.; Brudvig, G. W. *Biochemistry* **2001**, *40*, 7937–7945.

(29) Messinger, J.; Badger, M.; Wydrzynski, T. *Proc. Natl. Acad. Sci. U.S.A.* **1995**, *92*, 3209–3213.

(30) Beckmann, K.; Messinger, J.; Badger, M. R.; Wydrzynski, T.; Hillier, W. *Photosynth. Res.* **2009**, *102*, 511–522.

(31) Hendry, G.; Wydrzynski, T. *Biochemistry* **2003**, *42*, 6209–6217.

(32) Hillier, W.; McConnell, I.; Singh, S.; Debus, R.; Boussac, A.; Wydrzynski, T. *Photosynthesis. Energy from the Sun* **2008**, 427–430.

(33) Kargul, J.; Maghlaoul, K.; Murray, J. W.; Deak, Z.; Boussac, A.; Rutherford, A. W.; Vass, I.; Barber, J. *Biochim. Biophys. Acta* **2007**, *1767*, 404–413.

(34) Ishida, N.; Sugiura, M.; Rappaport, F.; Lai, T. L.; Rutherford, A. W.; Boussac, A. *J. Biol. Chem.* **2008**, *283*, 13330–13340.

(35) Pushkar, Y. L.; Yano, J.; Sauer, K.; Boussac, A.; Yachandra, V. K. *Proc. Natl. Acad. Sci.* **2008**, *105*, 1879–1884.

(36) Latimer, M. J.; DeRose, V. J.; Mukerji, I.; Yachandra, V. K.; Sauer, K.; Klein, M. P. *Biochemistry* **1995**, *34*, 10898–10909.

(37) Latimer, M. J.; DeRose, V. J.; Yachandra, V. K.; Sauer, K.; Klein, M. P. *J. Phys. Chem. B* **1998**, *102*, 8257–8265.

(38) Cinco, R. M.; McFarlane Holman, K. L.; Robblee, J. H.; Yano, J.; Pizarro, S. A.; Bellacchio, E.; Sauer, K.; Yachandra, V. K. *Biochemistry* **2002**, *41*, 12928–12933.

(39) Cinco, R. M.; Robblee, J. H.; Rompel, A.; Fernandez, C.; Yachandra, V. K.; Sauer, K.; Klein, M. P. *J. Phys. Chem. B* **1998**, *102*, 8248–8256.

(40) Robblee, J. H.; Cinco, R. M.; Yachandra, V. K. *Biochim. Biophys. Acta* **2001**, *1503*, 7–23.

(41) Cinco, R. M.; Robblee, J. H.; Messinger, J.; Fernandez, C.; McFarlane Holman, K. L. M.; Sauer, K.; Yachandra, V. K. *Biochemistry* **2004**, *43*, 13271–13282.

(42) *A new crystal structure was recently disclosed by Jian-Ren Shen (Okayama University, Japan) at the 15th International Congress of Photosynthesis. This new structure has yet to be published and, as such, is not explicitly considered in this manuscript. It is noted that the structure of the OEC reported is most similar to the Siegbahn structure (Figure 1 F).*

(43) Sproviero, E. M.; Gascón, J. A.; McEvoy, J. P.; Brudvig, G. W.; Batista, V. S. *J. Chem. Theory Comput.* **2006**, *2*, 1119–1134.

(44) Sproviero, E. M.; Gascón, J. A.; McEvoy, J. P.; Brudvig, G. W.; Batista, V. S. *J. Am. Chem. Soc.* **2008**, *130*, 6728–6730.

(45) Sproviero, E. M.; Gascón, J. A.; McEvoy, J. P.; Brudvig, G. W.; Batista, V. S. *Curr. Opin. Struct. Biol.* **2007**, *17*, 173–180.

(46) Yachandra, V.; DeRose, V.; Latimer, M.; Mukerji, I.; Sauer, K.; Klein, M. *Science* **1993**, *260*, 675–679.

(47) Yachandra, V. K.; Sauer, K.; Klein, M. P. *Chem. Rev.* **1996**, *96*, 2927–2950.

(48) Robblee, J. H.; Messinger, J.; Cinco, R. M.; McFarlane, K. L.; Fernandez, C.; Pizarro, S. A.; Sauer, K.; Yachandra, V. K. *J. Am. Chem. Soc.* **2002**, *124*, 7459–7471.

(49) Murray, J. W.; Maghlaoui, K.; Kargul, J.; Ishida, N.; Lai, T.-L.; Rutherford, A. W.; Sugiura, M.; Boussac, A.; Barber, J. *Energy Environ. Sci.* **2008**, *1*, 161–166.

(50) van Gorkom, H. J.; Yocum, C. F. *The calcium and chloride cofactors*; Springer, 2005; Vol. 1.

(51) Kawakami, K.; Umena, Y.; Kamiya, N.; Shen, J. R. *Proc. Natl. Acad. Sci. U.S.A.* **2009**, *106*, 8567–8572.

(52) Haumann, M.; Barra, M.; Loja, P.; Löscher, S.; Krivanek, R.; Grundmeier, A.; Andreassen, L. E.; Dau, H. *Biochemistry* **2006**, *45*, 13101–13107.

(53) Petrie, S.; Stranger, R.; Gatt, P.; Pace, R. J. *Chem.—Eur. J.* **2007**, *13*, 5082–5089.

(54) Petrie, S.; Stranger, R.; Pace, R. J. *Chem.—Eur. J.* **2008**, *14*, 5482–5494.

(55) Kusunoki, M. *Biochim. Biophys. Acta* **2007**, *1767*, 484–492.

(56) Zein, S.; Kulik, L. V.; Yano, J.; Kern, J.; Pushkar, Y.; Zouni, A.; Yachandra, V. K.; Lubitz, W.; Neese, F.; Messinger, J. *Philos. Trans. R. Soc.* **2008**, *363*, 1167–1177.

(57) Pantazis, D. A.; Orio, M.; Petrenko, T.; Zein, S.; Lubitz, W.; Messinger, J.; Neese, F. *Phys. Chem. Chem. Phys.* **2009**, *11*, 6788–6798.

(58) Siegbahn, P. E. M. *Chem.—Eur. J.* **2008**, *14*, 8290–8302.

(59) Siegbahn, P. E. M. *J. Am. Chem. Soc.* **2009**, *131*, 18238–18239.

(60) Dau, H.; Grundmeier, A.; Loja, P.; Haumann, M. *Philos. Trans. R. Soc., B* **2008**, *363*, 1237–1244.

(61) Dau, H.; Haumann, M. *Coord. Chem. Rev.* **2008**, *252*, 273–295.

(62) Horner, O.; Rivière, E.; Blondin, G.; Un, S.; Rutherford, A. W.; Girerd, J.-J.; Boussac, A. *J. Am. Chem. Soc.* **1998**, *120*, 7924–7928.

(63) Kulik, L.; Epel, B.; Messinger, J.; Lubitz, W. *Photosynth. Res.* **2005**, *84*, 347–353.

(64) Kulik, L. V.; Epel, B.; Lubitz, W.; Messinger, J. *J. Am. Chem. Soc.* **2005**, *127*, 2392–2393.

(65) Kulik, L. V.; Epel, B.; Lubitz, W.; Messinger, J. *J. Am. Chem. Soc.* **2007**, *129*, 13421–13435.

(66) Lorigan, G. A.; Britt, R. D. *Biochemistry* **1994**, *33*, 12072–12076.

(67) Peloquin, J. M.; Campbell, K. A.; Randall, D. W.; Evanchik, M. A.; Pecoraro, V. L.; Armstrong, W. H.; Britt, R. D. *J. Am. Chem. Soc.* **2000**, *122*, 10926–10942.

(68) Sivaraja, M.; Tso, J.; Dismukes, G. C. *Biochemistry* **1989**, *28*, 9459–9464.

(69) Sugiura, M.; Boussac, A.; Noguchi, T.; Rappaport, F. *Biochim. Biophys. Acta* **2008**, *1777*, 331–342.

(70) Sugiura, M.; Rappaport, F.; Brettel, K.; Noguchi, T.; Rutherford, A. W.; Boussac, A. *Biochemistry* **2004**, *43*, 13549–13563.

(71) Epel, B.; Gromov, I.; Stoll, S.; Schweiger, A.; Goldfarb, D. *Concepts Magn. Reson., Part B* **2005**, *26B*, 36–45.

(72) Stoll, S.; Schweiger, A. *J. Magn. Reson.* **2006**, *178*, 42–55.

(73) Becke, A. D. *Phys. Rev. A* **1988**, *38*, 3098–3100.

(74) Perdew, J. P. *Phys. Rev. B* **1986**, *33*, 8822–8824.

(75) Schäfer, A.; Huber, C.; Ahlrichs, R. *J. Chem. Phys.* **1994**, *100*, 5829–5835.

(76) Weigend, F. *Phys. Chem. Chem. Phys.* **2006**, *8*, 1057–1065.

(77) Neese, F. Universität Bonn: Bonn, Germany, 2007.

(78) Noodleman, L. *J. Chem. Phys.* **1981**, *74*, 5737–5743.

(79) Noodleman, L.; Case, D. A. *Adv. Inorg. Chem.* **1992**, *38*, 423–470.

(80) Noodleman, L.; Davidson, E. R. *Chem. Phys.* **1986**, *109*, 131–143.

(81) Neese, F. *Coord. Chem. Rev.* **2009**, *253*, 526–563.

(82) Staroverov, V. N.; Scuseria, G. E.; Tao, J.; Perdew, J. P. *J. Chem. Phys.* **2003**, *119*, 12129–12137.

(83) Neese, F.; Wennmohs, F.; Hansen, A.; Becker, U. *Chem. Phys.* **2009**, *356*, 98–109.

(84) van Wüllen, C. *J. Chem. Phys.* **1998**, *109*, 392–399.

(85) van Lenthe, E.; Snijders, J. G.; Baerends, E. J. *J. Chem. Phys.* **1996**, *105*, 6505–6516.

(86) Pantazis, D. A.; Chen, X. Y.; Landis, C. R.; Neese, F. *J. Chem. Theory Comput.* **2008**, *4*, 908–919.

(87) Sinnecker, S.; Neese, F.; Noodleman, L.; Lubitz, W. *J. Am. Chem. Soc.* **2004**, *126*, 2613–2622.

(88) Orio, M.; Pantazis, D. A.; Petrenko, T.; Neese, F. *Inorg. Chem.* **2009**, *48*, 7251–7260.

(89) Pantazis, D. A.; Krewald, V.; Orio, M.; Neese, F. *Dalton Trans.* **2010**, *39*, 4959–4967.

(90) Baffert, C.; Orio, M.; Pantazis, D. A.; Duboc, C.; Blackman, A. G.; Blondin, G.; Neese, F.; Deronzier, A.; Collomb, M.-N. *Inorg. Chem.* **2009**, *48*, 10281–10288.

(91) Pantazis, D. A.; Orio, M.; Petrenko, T.; Zein, S.; Bill, E.; Lubitz, W.; Messinger, J.; Neese, F. *Chem.—Eur. J.* **2009**, *15*, 5108–5123.

(92) Messinger, J.; Robblee, J. H.; Bergmann, U.; Fernandez, C.; Glatzel, P.; Visser, H.; Cinco, R. M.; McFarlane, K. L.; Bellacchio, E.; Pizarro, S. A.; Cramer, S. P.; Sauer, K.; Klein, M. P.; Yachandra, V. K. *J. Am. Chem. Soc.* **2001**, *123*, 7804–7820.

(93) Haumann, M.; Müller, C.; Liebisch, P.; Iuzzolino, L.; Dittmer, J.; Grabolle, M.; Neisius, T.; Meyer-Klaucke, W.; Dau, H. *Biochemistry* **2005**, *44*, 1894–1908.

(94) Boussac, A.; Sugiura, M.; Inoue, Y.; Rutherford, A. W. *Biochemistry* **2000**, *39*, 13788–13799.

(95) Beck, W. F.; de Paula, J. C.; Brudvig, G. W. *J. Am. Chem. Soc.* **1986**, *108*, 4018–4022.

(96) Randall, D. W.; Sturgeon, B. E.; Ball, J. A.; Lorigan, G. A.; Chan, M. K.; Klein, M. P.; Armstrong, W. H.; Britt, R. D. *J. Am. Chem. Soc.* **1995**, *117*, 11780–11789.

(97) Tso, J.; Sivaraja, M.; Dismukes, G. C. *Biochemistry* **1991**, *30*, 4734–4739.

(98) Boussac, A.; Rutherford, A. W.; Styring, S. *Biochemistry* **1990**, *29*, 24–32.

(99) Boussac, A.; Kuhl, H.; Ghibaudi, E.; Rögner, M.; Rutherford, A. W. *Biochemistry* **1999**, *38*, 11942–11948.

(100) Kulik, L. V.; Lubitz, W.; Messinger, J. *Biochemistry* **2005**, *44*, 9368–9374.

(101) Pudollek, S.; Lendzian, F.; Bittl, R. *Biochem. Soc. Trans.* **2008**, *36*, 1001–1004.

(102) Teutloff, C.; Kessen, S.; Kern, J.; Zouni, A.; Bittl, R. *FEBS Lett.* **2006**, *580*, 3605–3609.

(103) Bergmann, U.; Grush, M. M.; Horne, C. R.; DeMarois, P.; Penner-Hahn, J. E.; Yocum, C. F.; Wright, D. W.; Dubé; Armstrong, W. H.; Christou, G.; Eppley, H. J.; Cramer, S. P. *J. Phys. Chem. B* **1998**, *102*, 8350–8352.

(104) Roelofs, T. A.; Liang, W.; Latimer, M. J.; Cinco, R. M.; Rompel, A.; Andrews, J. C.; Sauer, K.; Yachandra, V. K.; Klein, M. P. *Proc. Natl. Acad. Sci. U.S.A.* **1996**, *93*, 3335–3340.

(105) Schäfer, K. O.; Bittl, R.; Zweygart, W.; Lendzian, F.; Haselhorst, G.; Weyhermüller, T.; Wieghardt, K.; Lubitz, W. *J. Am. Chem. Soc.* **1998**, *120*, 13104–13120.

(106) Zheng, M.; Dismukes, G. C. *Inorg. Chem.* **1996**, *35*, 3307–3319.

(107) Zheng, M.; Khangulov, S. V.; Dismukes, G. C.; Barynin, V. V. *Inorg. Chem.* **1994**, *33*, 382–387.

(108) Wiberg, E.; Hollerman, A. F.; Wiberg, N. *Lehrbuch der Anorganischen Chemie*; Walter de Gruyter GmbH & Co: Berlin, 2009.

(109) Yocum, C. F. *Coord. Chem. Rev.* **2008**, *252*, 296–305.

(110) Charlot, M.-F.; Boussac, A.; Blondin, G. *Biochim. Biophys. Acta* **2005**, *1708*, 120–132.

(111) Hasegawa, K.; Ono, T. A.; Kusunoki, M. *Bull. Chem. Soc. Jpn.* **1999**, *72*, 1013–1023.

(112) DeRose, V. J.; Mukerji, I.; Latimer, M. J.; Yachandra, V. K.; Sauer, K.; Klein, M. P. *J. Am. Chem. Soc.* **1994**, *116*, 5239–5249.

(113) Hasegawa, K.; Ono, T.-A.; Inoue, Y.; Kusunoki, M. *Chem. Phys. Lett.* **1999**, *300*, 9–19.

(114) Britt, R. D.; Campbell, K. A.; Peloquin, J. M.; Gilchrist, M. L.; Aznar, C. P.; Dicus, M. M.; Robblee, J.; Messinger, J. *Biochim. Biophys. Acta* **2004**, *1655*, 158–171.

(115) Carrell, T. G.; Tyryshkin, A.; Dismukes, G. C. *J. Biol. Inorg. Chem.* **2002**, *7*, 2–22.

(116) Baldwin, M. J.; Stemmler, T. L.; Riggs-Gelasco, P. J.; Kirk, M. L.; Penner-Hahn, J. E.; Pecoraro, V. L. *J. Am. Chem. Soc.* **1994**, *116*, 11349–11356.

(117) Debus, R. J.; Strickler, M. A.; Walker, L. M.; Hillier, W. *Biochemistry* **2005**, *44*, 1367–1374.

(118) Chu, H.-A.; Hillier, W.; Debus, R. J. *Biochemistry* **2004**, *43*, 3152–3166.

(119) Debus, R. J.; Aznar, C.; Campbell, K. A.; Gregor, W.; Diner, B. A.; Britt, R. D. *Biochemistry* **2003**, *42*, 10600–10608.

(120) *The labels Mn_C and Mn_D are arbitrary from an electronic perspective. They depend on the labeling of the specific exchange pathways within the cluster. They represent the same electronic structural position for the Mn^{III}; a corner of the trimer/triangle unit (Mn_B, Mn_C, Mn_D) that does not link the trimer to the external Mn (Mn_A).*

(121) Schäfer, K. O. Doctoral Thesis, Technische Universität Berlin, 2002.

(122) Griffith, J. S. *The theory of Transition-Metal Ions*; Cambridge University Press: London, 1971.

(123) Abragram, A.; Bleaney, B. *Electron Paramagnetic Resonance of Transition Metal Ions*; Clarendon Press: Oxford, 1970.

(124) Carrington, A.; McLachlan, A. D. *Introduction to Magnetic Resonance*; 1st ed.; Harper and Row: New York, 1967.

(125) Gerritsen, H. J.; Sabisky, E. S. *Phys. Rev.* **1963**, *132*.

(126) Campbell, K. A.; Force, D. A.; Nixon, P. J.; Dole, F.; Diner, B. A.; Britt, R. D. *J. Am. Chem. Soc.* **2000**, *122*, 3754–3761.

(127) Mossin, S.; Weihe, H.; Barra, A.-L. *J. Am. Chem. Soc.* **2002**, *124*, 8764–8765.

(128) Schinzel, S.; Schraut, J.; Arbuznikov, A.; Siegbahn, P. E. M.; Kaupp, M. *Chem.—Eur. J.* **2010**, *16*, 10424–10438.

(129) Boussac, A.; Girerd, J.-J.; Rutherford, A. *Biochemistry* **1996**, *35*, 6984–6989.

(130) Zimmermann, J. L.; Rutherford, A. W. *Biochemistry* **1986**, *25*, 4609–4615.

(131) Åhrling, K. A.; Evans, M. C. W.; Nugent, J. H. A.; Pace, R. J. *Biochim. Biophys. Acta, Bioenerg.* **2004**, *1656*, 66–77.

(132) Force, D. A.; Randall, D. W.; Lorigan, G. A.; Clemens, K. L.; Britt, R. D. *J. Am. Chem. Soc.* **1998**, *120*, 13321–13333.

(133) Åhrling, K. A.; Evans, M. C. W.; Nugent, J. H. A.; Ball, R. J.; Pace, R. J. *Biochemistry* **2006**, *45*, 7069–7082.

(134) Pace, R. J.; Smith, P. J.; Bramley, R.; Stehlik, D. *Biochim. Biophys. Acta* **1991**, *1058*, 161–170.

(135) Messinger, J. *Phys. Chem. Chem. Phys.* **2004**, *6*, 4764–4771.

(136) Petrie, S.; Stranger, R.; Pace, R. J. *Angew. Chem.* **2010**, *122*, 4329–4332.

3648

dx.doi.org/10.1021/ja110145v |*J. Am. Chem. Soc.* 2011, 133, 3635–3648